

Localized defect states in two-dimensional photonic crystal slab waveguides: A simple model based upon symmetry analysis

Oskar Painter* and Kartik Srinivasan

Department of Applied Physics, California Institute of Technology, Pasadena, California 91125, USA

(Received 31 December 2002; published 17 July 2003)

Localized defect regions within two-dimensional photonic crystal slab waveguides are an attractive method of forming high-quality factor optical resonators with wavelength-scale modal volumes. Using simple symmetry bases, and the tools of group theory, we develop an approximate description of the resonant modes of different photonic crystal defect cavities. Comparison to numerical simulations as well as photoluminescence measurements of actual microfabricated devices demonstrates the power of this modest symmetry analysis in describing the localized defect states within photonic crystals.

DOI: 10.1103/PhysRevB.68.035110

PACS number(s): 42.70.Qs, 42.55.Sa, 42.60.Da, 42.55.Px

I. INTRODUCTION

Planar two-dimensional (2D) photonic crystal (PC) slab waveguide (WG) structures^{1–3} have been the focus of much research in recent years since they are a promising architecture for future generations of high-density lightwave circuits. In-plane waveguides,^{4–7} coupled-resonator-waveguide systems,^{8–10} and add-drop devices^{11,12} are amongst the devices in which recent progress has been made. Another area of particular interest is the development of wavelength-scale mode volume, high-quality (high- Q) factor optical resonators within PC slab WGs. In such structures, local modifications (defects) of the photonic lattice have been used to form nanometer-scale lasers which trap light to volumes close to the theoretical limit of a cubic half wavelength.^{13–16} Advances in fabrication have reached the point where planar lithography allows for the precise control of the defect geometry in these systems.¹⁷ Such control has been used to create optical cavities with defect mode resonances of a given polarization, frequency, and emission pattern.¹⁸

The design of PC-based optical elements has often relied on numerical simulations using methods such as finite-difference time domain (FDTD).¹⁴ While FDTD provides a wealth of detailed information about the system under consideration, it has the drawback of being rather computationally intensive and time consuming. In this paper an approximate analytic technique is presented which uses symmetry and the methods of group theory to analyze and classify the modes of resonant cavities formed in 2D PC slab WG structures. This technique determines the symmetry of the modes that form and their dominant Fourier components, from which one can extract information regarding the far-field emission pattern as well as the polarization of the resonant modes. The symmetry analysis can also be used as a tool in designing high- Q cavity modes¹⁹ and low-loss waveguides²⁰ in 2D PC slabs, predicting the type of crystal lattice and the position of point and linear defects within the crystal which will produce localized modes with reduced in-plane and vertical loss.

The principle thrust of the paper is contained in Sec. II, which outlines the application of group theory in producing an approximate description of the resonant modes of the de-

fect cavities in hexagonal and square host photonic lattices. Section III then presents the results of FDTD simulations, confirming the results of the approximate group-theory analysis while providing detailed properties of the defect mode resonances beyond the scope of the simple symmetry analysis. Experimental data in the form of spectroscopic probing through photoluminescence (PL) measurements of fabricated devices are also given, completing a study of these devices that began at the very fundamental level of examining their symmetries.

II. SYMMETRY ANALYSIS

The spatial symmetries within Maxwell's equations are determined by the translation and rotary-reflection symmetries of the dielectric function, $\epsilon(\mathbf{r})$.^{21,22} The theory of space groups²³ can then be used to predict and categorize the resonant modes of defects within PC structures. A two-step process is implemented here. First, modes of the unperturbed slab waveguide are used as a symmetry basis to generate approximate field patterns for the PC modes at the high-symmetry points of the first Brillouin zone (IBZ) boundary. The curvature of the photonic bands at these points are such that peaks and valleys are created in the energy-momentum dispersion surface. Invoking an equivalent Wannier theorem for photons²⁴ one can argue that it is these peaks and valleys that are the seeds from which localized states are formed (see the Appendix). The second step in our approach then utilizes the PC band-edge states created from the unperturbed slab waveguide mode symmetry basis to generate approximate forms for the localized defect modes lying within the band gap.

The host PC structures that we consider in this paper consist of a symmetric planar geometry with a two-dimensionally patterned core layer surrounded by spatially uniform cladding layers. A structure which has been the basis of many previously fabricated devices¹⁶ is depicted in cross section in Fig. 1(a). The semiconductor core dielectric material has an approximate refractive index of 3.4, and the cladding in these *membrane*-type structures is air with a refractive index of 1. For the structures studied in this and the following sections, the ratio of the core thickness, d , to lattice parameter, a , is chosen so as to maintain the single-mode

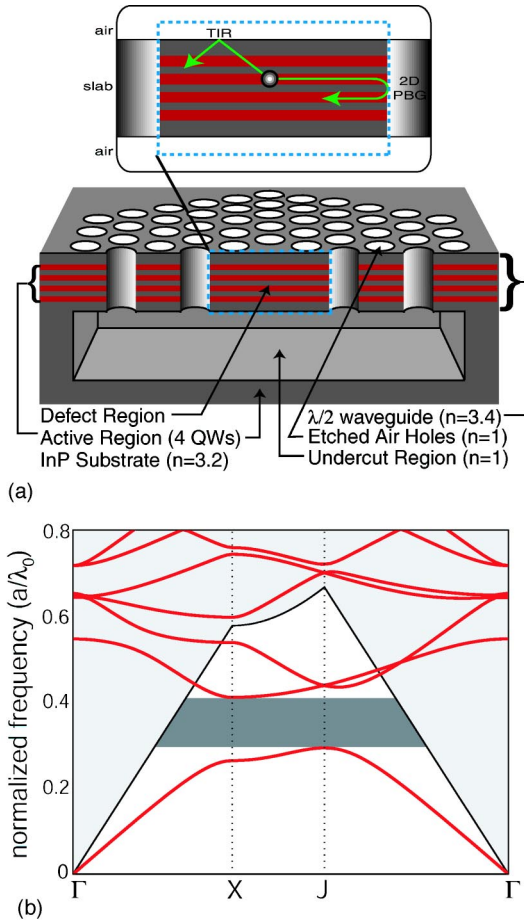


FIG. 1. (a) Illustration of the two-dimensional hexagonal PC slab waveguide structure. (b) In-plane band structure; fundamental TE-like (even) guided-mode band structure ($r/a=0.36, n_{\text{slab}}=n_{\text{eff}}=2.65$). The guided-mode band gap extends over a normalized frequency of 0.29–0.41. The air (cladding) light line is shown as a solid black line.

nature of the vertical waveguide for wavelengths within the first-order guided-mode band gap of the PC lattice. The modes of a symmetric slab waveguide, patterned or unpatterned, separate into modes of even or odd parity with respect to a mirror plane in the middle of the dielectric slab. Of interest here are the *fundamental* guided modes, which for the slab thicknesses of the devices analyzed in Sec. III, have a wavelength commensurate with the emission band of the quantum wells. Limiting our analysis to the fundamental guided modes of the PC slab effectively reduces the spatial dimension of the problem from three to two.

For these symmetric quasi-2D systems, within the mirror plane of the waveguide the fundamental even and odd modes can be represented by scalar fields B_z and E_z , respectively. As has been described elsewhere,²⁵ for connected 2D lattices such as those investigated here the extent of the photonic band gap for modes with electric-field polarization in the plane of the 2D patterning (TE) is larger than for modes with normal electric-field polarization (TM). Although the fundamental even and odd modes of the quasi-2D patterned slab are not purely TE or TM polarized they are significantly TE-like or TM-like in nature, respectively. For this reason,

and the fact that the active region of the light-emitting devices studied in Sec. III predominantly couples to TE polarized light,²⁶ we will focus our attention in this paper on the fundamental even modes of the 2D PC waveguides which are TE-like. In the analysis below we consider for the host PC lattice two of the most common 2D geometries, the square lattice and the hexagonal or trigonal lattice. We begin with an analysis of the hexagonal lattice.

A. Hexagonal lattice

The point-group symmetry of a 2D hexagonal PC is D_{6h} . Extruding the 2D PC into a symmetric 3D waveguide structure gives a single horizontal mirror plane (σ_h) lying in the waveguide center. As alluded to above, for the hexagonal PC slab waveguide of Fig. 1(a), a band gap opens up in the frequency spectrum of the fundamental even guided modes, but not in the fundamental odd mode spectrum.¹⁴ Narrowing our scope to TE-like modes of a symmetric slab, the point-group symmetry of the hexagonal PC system can be effectively reduced to $C_{6v}=D_{6h}/\sigma_h$. A plot of the approximate²⁷ in-plane band structure for the fundamental TE-like guided modes of a half-wavelength thick hexagonally patterned slab waveguide is given in Fig. 1(b).

For the TE-like fundamental even eigenmodes of the unpatterned slab waveguide, within the mirror plane of the slab the magnetic-field pattern can be written as $\mathbf{B}_{\mathbf{k}_{\perp}}(\mathbf{r}_{\perp}) = \hat{z}e^{-i(\mathbf{k}_{\perp}\cdot\mathbf{r}_{\perp})}$, where \mathbf{k}_{\perp} and \mathbf{r}_{\perp} are in-plane wave-number and spatial coordinates, respectively (in order to simplify notation we drop the \perp label in the equations which follow). Upon patterning the slab waveguide, coupling occurs between waveguide modes with similar unperturbed frequencies and identical propagation constants modulo a reciprocal-lattice vector \mathbf{G} . This follows from the approximate conservation of frequency (kinematic treatment) and the exact conservation of crystal momentum. Of particular interest for the resonant-cavity designs and devices described below are those modes which comprise the frequency bands defining the first-order band gap. The Bloch modes at the band edges defining the first-order band gap are predominantly formed from modes of the unpatterned waveguide with the in-plane wave vector lying at the boundary of the IBZ; other unpatterned waveguide modes with additional in-plane momentum equal to some integer multiple of a reciprocal-lattice vector contribute much less, owing to their large (unperturbed) frequency difference. For the symmetry analysis described here we will be satisfied with considering the contribution from only the degenerate lowest-frequency unpatterned waveguide modes at the first zone boundary.

The high-symmetry points within and on the boundary of the IBZ of the hexagonal lattice are [see Fig. 2(b)] the six X points [$\{\pm(0,1)k_X, \pm(\sqrt{3}/2, 1/2)k_X, \pm(\sqrt{3}/2, -1/2)k_X\}$], the six J points [$\{\pm(1/2, \sqrt{3}/2)k_J, \pm(1/2, -\sqrt{3}/2)k_J, \pm(1,0)k_J\}$], and the Γ point (0,0). The first-order band gap of the hexagonal lattice [see Fig. 1(b)] is defined from above by the X point and below by the J point. In analogy to the electronic bands in semiconductor crystals we term the high-frequency band defining the first-order band gap the “conduction” band, and the low-frequency band the “valence”

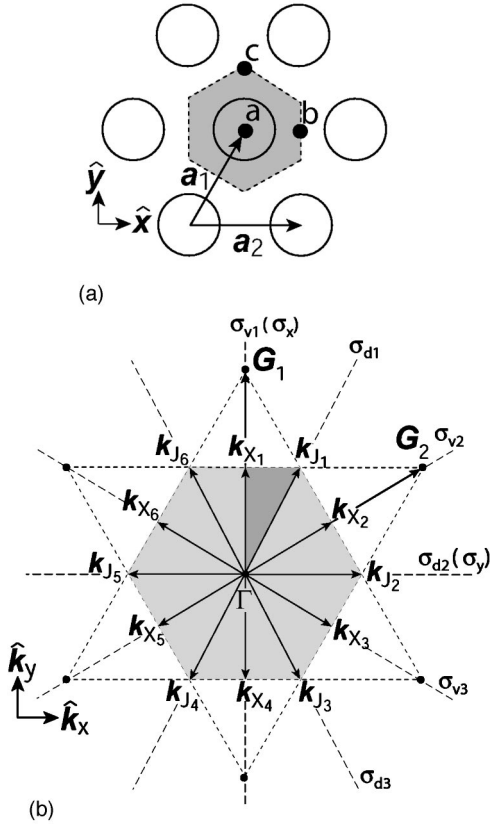


FIG. 2. Illustrations of the real and reciprocal spaces of the two-dimensional hexagonal PC. The high-symmetry points of the hexagonal lattice, referenced to the center of an air hole, are $\mathbf{a} = (0,0)$, $\mathbf{b} = (a/2,0)$, and $\mathbf{c} = (0,a/\sqrt{3})$. (a) Real-space lattice. $|\mathbf{a}_1| = |\mathbf{a}_2| = a$. (b) Reciprocal space. $|\mathbf{G}_1| = |\mathbf{G}_2| = 4\pi/\sqrt{3}a$, $|\mathbf{k}_X| = 2\pi/\sqrt{3}a$, and $|\mathbf{k}_J| = 4\pi/3a$.

band. In the approximate analysis of the defect states to follow we will need to include all the degenerate satellite peaks (conduction band) and valleys (valence band). The group of the wave vector, which defines the point-group symmetry of a plane-wave modulo \mathbf{G} within the dielectric lattice, is for the X , J , and Γ points of the hexagonal lattices C_{2v} , C_{3v} , and C_{6v} , respectively. Character tables²⁸ for these groups are given in Table I.

1. X point

For the frequency bands defining the first-order band gap, the unpatterned waveguide modes which are most strongly coupled together to form the Bloch modes at the X point are in our quasi-2D picture given by $\mathbf{B} = \hat{z} e^{-i\mathbf{k}_{X_i} \cdot \mathbf{r}}$, where $i = 1, 2, \dots, 6$. The unperturbed frequencies of these modes are degenerate and can be written as $\omega_o^X \approx c|\mathbf{k}_{X_i}|/n_{\text{eff}}$, where n_{eff} is an effective index taking into account the vertical waveguiding perpendicular to the slab.

The star of \mathbf{k} ($*\mathbf{k}$) at the X point, formed from the independent satellite X points within the IBZ, consists (not uniquely) of wave vectors $\{\mathbf{k}_{X_1}, \mathbf{k}_{X_2}, \mathbf{k}_{X_3}\}$, all other X points being equivalent to one of these vectors modulo a reciprocal-lattice vector. A symmetry basis for the modes of the pat-

TABLE I. Point-group character tables.

C_{6v}	E	C_2	$2C_3$	$2C_6$	$3\sigma_d$	$3\sigma_v$
A_1''	1	1	1	1	1	1
A_2''	1	1	1	1	-1	-1
B_1''	1	-1	1	-1	1	-1
B_2''	1	-1	1	-1	-1	1
E_1	2	-2	-1	1	0	0
E_2	2	2	-1	-1	0	0
$S^{a,d1}$	3	-3	0	0	1	-1
$S^{a,a1}$	2	0	2	0	-2	0
$S^{a,a2}$	3	3	0	0	-1	-1
C_{2v}	E	C_2	$\sigma_x(\sigma_{v1})$	$\sigma_y(\sigma_{d2})$		
A_1	1	1	1	1		
A_2	1	1	-1	-1		
B_1	1	-1	-1	1		
B_2	1	-1	1	-1		
$S^{a,d1}$	3	-3	-1	1		
$S^{b,d1}$	3	1	-1	1		
$S^{a,a1}$	2	0	0	-2		
$S^{a,a2}$	3	3	-1	-1		
$S^{b,a1}$	3	3	-1	-1		
C_{3v,σ_d}	E	$2C_3$	$3\sigma_d$			
A_1'	1	1	1			
A_2'	1	1	-1			
E	2	-1	0			
C_{3v,σ_v}	E	$2C_3$	$3\sigma_v$			
A_1'''	1	1	1			
A_2'''	1	1	-1			
E	2	-1	0			
$S^{c,d1}$	3	0	-1			
$S^{c,a1}$	2	-1	0			

terned slab waveguide at the X_1 -satellite point, the irreducible representations (IRREPs) of the little group at the X point, can be found by applying the symmetry operations of the group of the wave vector ($\mathcal{G}_{\mathbf{k}_{X_1}} = C_{2v}$) to the seed vector $\mathbf{B}_{\mathbf{k}_{X_1}}$. In this case, the basis is simply $(\mathbf{B}_{\mathbf{k}_{X_1}}, \mathbf{B}_{-\mathbf{k}_{X_1}})$. Projecting this symmetry basis onto the IRREP spaces of C_{2v} yields

$$\begin{aligned} \mathbf{B}_{A_2}^{X_1} &= \hat{z} \cos(\mathbf{k}_{X_1} \cdot \mathbf{r}^a), \\ \mathbf{B}_{B_1}^{X_1} &= \hat{z} \sin(\mathbf{k}_{X_1} \cdot \mathbf{r}^a), \end{aligned} \quad (1)$$

where A_2 and B_1 label the IRREP spaces of C_{2v} (see Table I), and the index a is used to denote the location of the origin within the hexagonal lattice [marked in Fig. 2(a)]. Since the magnetic field of $\mathbf{B}_{A_2}^{X_1}$ overlaps strongly with the air holes of the hexagonal PC (its electric field lying largely in the di-

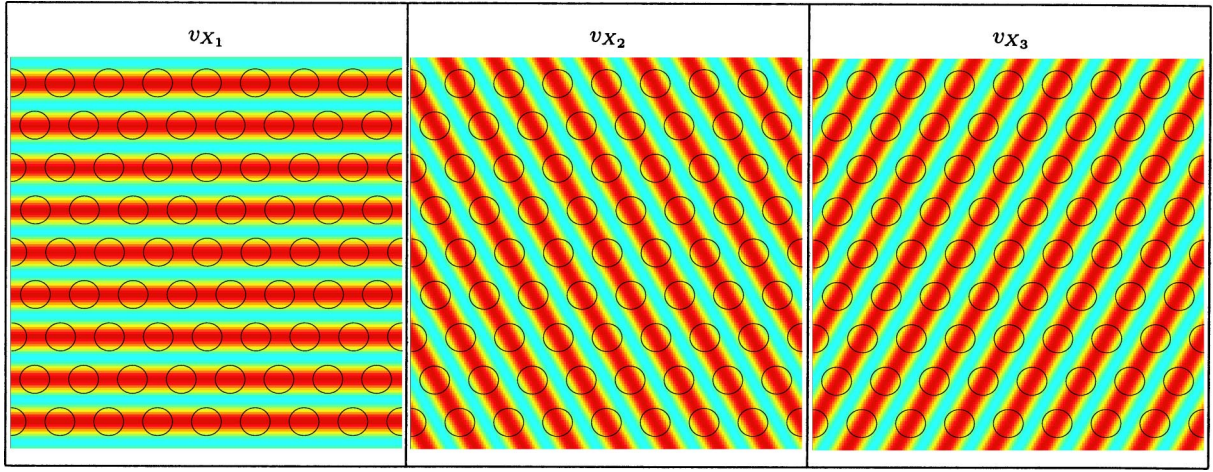


FIG. 3. Magnetic-field (amplitude) patterns of the valence-band modes of the hexagonal lattice at the three different X points generated by the symmetry basis VB_a^X .

electric) it represents the lower-frequency “valence”-band mode, while $B_{B_1}^{X_1}$ represents the “conduction”-band mode. This is a result of the tendency for modes with electric field concentrated within regions of high dielectric constant to be lower frequency than those with electric field concentrated in low dielectric regions.²⁵

In order to fully define the modes at the X point all modes of the $*\mathbf{k}$ must be included. The point symmetry operations of the full point group of the hexagonal lattice not included in the group of the wave vector, the coset generators, may be used to generate the modes of all the degenerate satellite points within the $*\mathbf{k}$. In the case of the X point this corresponds to successive rotations by $\pi/6$ (C_6 rotation). The result is the following set of degenerate valence-band modes,

$$VB_a^X = \begin{pmatrix} v_{X_1} \\ v_{X_2} \\ v_{X_3} \end{pmatrix} = \hat{z} \begin{bmatrix} \cos(\mathbf{k}_{X_1} \cdot \mathbf{r}^a) \\ \cos(\mathbf{k}_{X_2} \cdot \mathbf{r}^a) \\ \cos(\mathbf{k}_{X_3} \cdot \mathbf{r}^a) \end{bmatrix}, \quad (2)$$

and degenerate conduction-band modes,

$$CB_a^X = \begin{pmatrix} c_{X_1} \\ c_{X_2} \\ c_{X_3} \end{pmatrix} = \hat{z} \begin{bmatrix} \sin(\mathbf{k}_{X_1} \cdot \mathbf{r}^a) \\ \sin(\mathbf{k}_{X_2} \cdot \mathbf{r}^a) \\ \sin(\mathbf{k}_{X_3} \cdot \mathbf{r}^a) \end{bmatrix}. \quad (3)$$

Figures 3 and 4 show the magnetic-field amplitudes for each of the valence- and conduction-band modes at all the satellite X points of the hexagonal lattice.

2. J point

A similar procedure may be performed in order to determine approximate forms for the TE-like valence- and conduction-band modes of the hexagonal lattice at the J point of the IBZ. Approximate forms for the valence-band-edge and conduction-band-edge modes at the J point are (with point a taken as the origin):

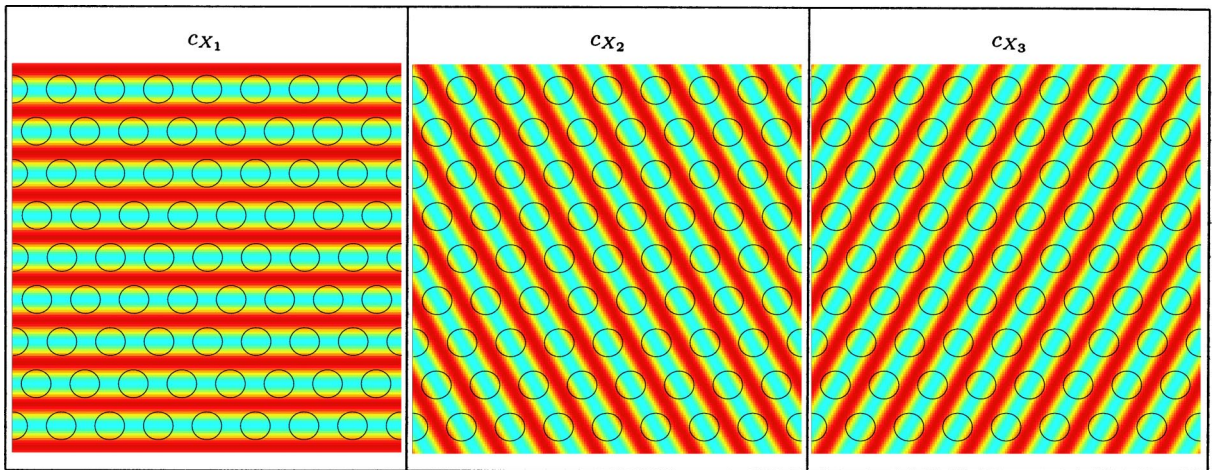


FIG. 4. Magnetic-field (amplitude) patterns of the conduction-band modes of the hexagonal lattice at the three different X points generated by the symmetry basis CB_a^X .

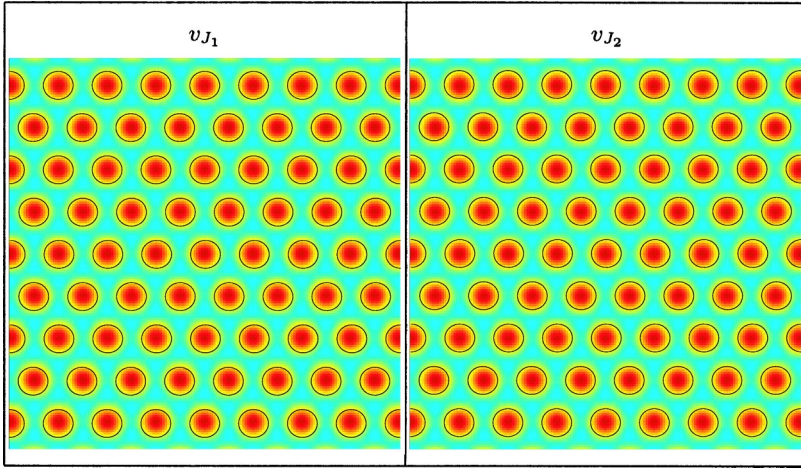


FIG. 5. Magnetic-field (amplitude) patterns of the valence-band modes of the hexagonal lattice at the J point generated by the symmetry basis VB_a^J .

$$VB_a^J = \begin{pmatrix} v_{J_1} \\ v_{J_2} \end{pmatrix} = \hat{z} \begin{pmatrix} e^{-ik_{J_1} \cdot \mathbf{r}^a} + e^{-ik_{J_3} \cdot \mathbf{r}^a} + e^{-ik_{J_5} \cdot \mathbf{r}^a} \\ e^{-ik_{J_2} \cdot \mathbf{r}^a} + e^{-ik_{J_4} \cdot \mathbf{r}^a} + e^{-ik_{J_6} \cdot \mathbf{r}^a} \end{pmatrix}, \quad (4)$$

$$CB_a^J = \begin{pmatrix} c1_{J_1} \\ c2_{J_1} \\ c1_{J_2} \\ c2_{J_2} \end{pmatrix} = \hat{z} \begin{pmatrix} e^{-ik_{J_1} \cdot \mathbf{r}^a} + e^{-ik_{J_3} \cdot \mathbf{r}^a} - 2e^{-ik_{J_5} \cdot \mathbf{r}^a} \\ e^{-ik_{J_1} \cdot \mathbf{r}^a} - e^{-ik_{J_3} \cdot \mathbf{r}^a} \\ e^{-ik_{J_2} \cdot \mathbf{r}^a} + e^{-ik_{J_4} \cdot \mathbf{r}^a} - 2e^{-ik_{J_6} \cdot \mathbf{r}^a} \\ e^{-ik_{J_2} \cdot \mathbf{r}^a} - e^{-ik_{J_4} \cdot \mathbf{r}^a} \end{pmatrix}. \quad (5)$$

Figures 5 and 6 show the magnetic-field amplitudes for each of the valence- and conduction-band modes at the J point of the hexagonal lattice. Although not obvious from first inspection of Eqs. (4) and (5), the plots in these two figures show that the modes of the symmetry basis VB_a^J have magnetic-field amplitude predominantly overlapping the air holes while the magnetic-field amplitudes of the modes of CB_a^J overlap the dielectric regions, a property that allows us to classify the modes as valence- and conduction-band, respectively. This result is also quite encouraging, given the fact that our symmetry basis is quite primitive and yet can reproduce this property of the valence- and conduction-band modes so critical to the formation of a frequency band gap.

The approximate valence- and conduction-band-edge modes derived above all have their origin at the center of an air hole of the lattice. The hexagonal lattice has two other high-symmetry points around which one may center a defect, points b and c shown in Fig. 2(a). Unlike point a , points b and c are of lower symmetry than the point group of the hexagonal lattice. A defect centered about point b will be limited to a point group of symmetry C_{2v} , and those about point c to point group C_{3v,σ_v} . The point-group symmetry operations for each of these types of defects are centered about *different* points within the lattice. So as to be clear about the position of the origin to be used for point symmetry operations, we label the Bloch mode symmetry bases with an index corresponding to the location of the origin around which it is expanded, the point symmetry operations assumed to act about this point. For example, VB_b^X is the X -point valence-band basis of Eq. (2) written in a shifted

coordinate system with point b at the origin. In the equations to follow, \mathbf{r}^a , \mathbf{r}^b , and \mathbf{r}^c are coordinate systems with origins located at points a , b , and c of the hexagonal lattice, respectively.

3. Conduction-band donor modes

In an attempt to form localized resonances, the dielectric constant in a small region of a periodic photonic crystal lattice may be altered from its unperturbed value, breaking the regular periodicity of the lattice and mixing the Bloch modes. If the perturbation corresponds to a local increase in the dielectric constant, then the localized modes are formed predominantly from the conduction-band modes, specifically the modes at the band edge. This is a result of the tendency for mode frequencies to decrease with increasing dielectric constant,²⁵ pulling the conduction-band-edge modes into the band gap of the photonic crystal near the defect. This type of localized mode is termed a donor mode in analogy to the electronic defect states in crystalline materials.

For the hexagonal PC lattice the minimum in the conduction band occurs at the X point [see Fig. 1(b)]. Therefore, the appropriate symmetry basis to use for describing localized donor modes are the degenerate conduction-band-edge modes of CB_a^X , CB_b^X , and CB_c^X for defect regions centered around points a , b , and c of the hexagonal lattice, respectively (note that these are all the same bases, just written in shifted coordinate systems). For defect regions centered about point a the largest possible symmetry is that of the underlying hexagonal lattice, C_{6v} , whereas for defects about point b and point c the largest point-group symmetries are C_{2v} and C_{3v,σ_v} , respectively. Correspondingly, the character values of representation $S^{a,d1}$ of the CB_a^X basis under C_{6v} , representation $S^{b,d1}$ of the CB_b^X basis under C_{2v} , and representation $S^{c,d1}$ of the CB_c^X basis under C_{3v,σ_v} are given in Table I. From the character tables we find that these representations decompose as $S^{a,d1} = E_1 \oplus B_1''$, $S^{b,d1} = A_1 \oplus A_2 \oplus B_1$, and $S^{c,d1} = E \oplus A_2'''$. Using the appropriate projection operators²⁸ on CB_a^X , CB_b^X , and CB_c^X , a set of basis functions for the localized conduction-band donor modes is found to be

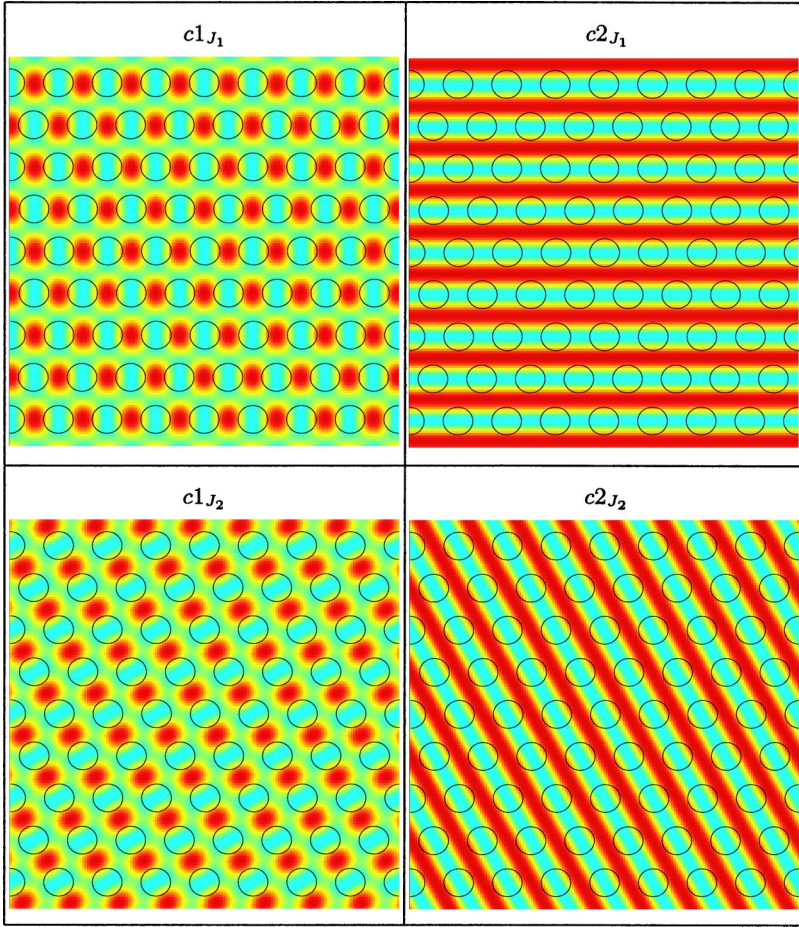


FIG. 6. Magnetic-field (amplitude) patterns of the conduction-band modes of the hexagonal lattice at the J point generated by the symmetry basis CB'_a .

$$\begin{aligned} \mathbf{B}_{B_1}^{a,d1} &= \hat{z}[\sin(\mathbf{k}_{X_1} \cdot \mathbf{r}^a) - \sin(\mathbf{k}_{X_2} \cdot \mathbf{r}^a) + \sin(\mathbf{k}_{X_3} \cdot \mathbf{r}^a)], \\ \mathbf{B}_{E_{1,1}}^{a,d1} &= \hat{z}[2 \sin(\mathbf{k}_{X_1} \cdot \mathbf{r}^a) + \sin(\mathbf{k}_{X_2} \cdot \mathbf{r}^a) - \sin(\mathbf{k}_{X_3} \cdot \mathbf{r}^a)], \\ \mathbf{B}_{E_{1,2}}^{a,d1} &= \hat{z}[\sin(\mathbf{k}_{X_2} \cdot \mathbf{r}^a) + \sin(\mathbf{k}_{X_3} \cdot \mathbf{r}^a)], \end{aligned} \quad (6)$$

for defects centered about point a of the hexagonal lattice,

$$\begin{aligned} \mathbf{B}_{A_1}^{b,d1} &= \hat{z}[\cos(\mathbf{k}_{X_2} \cdot \mathbf{r}^b) - \cos(\mathbf{k}_{X_3} \cdot \mathbf{r}^b)], \\ \mathbf{B}_{A_2}^{b,d1} &= \hat{z}[\cos(\mathbf{k}_{X_2} \cdot \mathbf{r}^b) + \cos(\mathbf{k}_{X_3} \cdot \mathbf{r}^b)], \\ \mathbf{B}_{B_1}^{b,d1} &= \hat{z}[\sin(\mathbf{k}_{X_1} \cdot \mathbf{r}^b)], \end{aligned} \quad (7)$$

for defects centered about point b , and

$$\begin{aligned} \mathbf{B}_{A_2}^{c,d1} &= \hat{z} \left[\sin\left(\mathbf{k}_{X_1} \cdot \mathbf{r}^c - \frac{\pi}{3}\right) - \sin\left(\mathbf{k}_{X_2} \cdot \mathbf{r}^c + \frac{\pi}{3}\right) \right. \\ &\quad \left. + \sin\left(\mathbf{k}_{X_3} \cdot \mathbf{r}^c - \frac{\pi}{3}\right) \right], \end{aligned}$$

$$\begin{aligned} \mathbf{B}_{E_{1,1}}^{c,d1} &= \hat{z} \left[2 \sin\left(\mathbf{k}_{X_1} \cdot \mathbf{r}^c - \frac{\pi}{3}\right) + \sin\left(\mathbf{k}_{X_2} \cdot \mathbf{r}^c + \frac{\pi}{3}\right) \right. \\ &\quad \left. - \sin\left(\mathbf{k}_{X_3} \cdot \mathbf{r}^c - \frac{\pi}{3}\right) \right], \\ \mathbf{B}_{E_{2,2}}^{c,d1} &= \hat{z} \left[\sin\left(\mathbf{k}_{X_2} \cdot \mathbf{r}^c + \frac{\pi}{3}\right) + \sin\left(\mathbf{k}_{X_3} \cdot \mathbf{r}^c - \frac{\pi}{3}\right) \right], \end{aligned} \quad (8)$$

for defects centered about point c . Figure 7 shows plots of the amplitude of the \hat{z} component of the magnetic field for each of the localized donor modes centered about point a of the hexagonal lattice generated by the symmetry analysis. The localized donor modes centered about points b and c are shown in Figs. 8 and 9, respectively.

In the above-mentioned plots of the defect modes (and in all plots generated from the symmetry analysis to follow), the localization of each mode has been taken into account by multiplying a two-dimensional Gaussian envelope function with each dominant Fourier component, where the two axes of the Gaussian envelope are taken as parallel and perpendicular to the direction of the Fourier component. This set of envelope function transforms as the identity under symmetry operations of the group of the wave vector, and as such does not alter the transformation properties of each \mathbf{k} component. Consequently, the IRREP classification of the defect modes given above is maintained. This particular choice of enve-

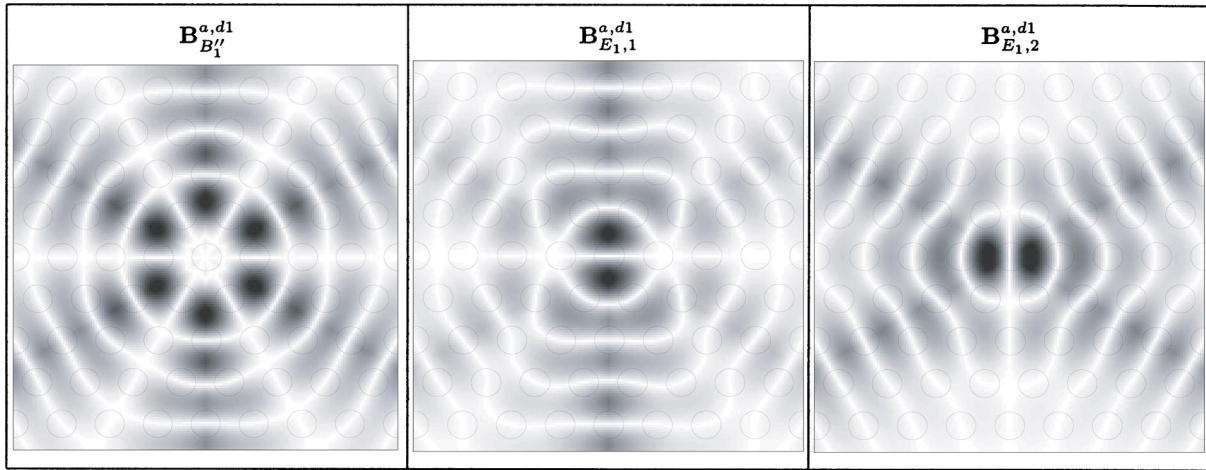


FIG. 7. Magnetic-field amplitude of the symmetry analysis conduction-band donor modes centered about point a of the hexagonal lattice.

lope function, apart from symmetry, is rather arbitrary, only chosen to capture the localized nature of the defect modes and highlight the dominant Fourier components. In the Appendix A, a Wannier-like equation for the envelope of localized photon states is studied and shown to have ground-state solutions invariant under those elements of the group of the wave vector that are also symmetries of the defect perturbation. The ground-state envelope solutions of the Appendix A, then, leave the IRREP classification of the above analysis for the defect modes unchanged.

From the form of the Wannier-like Eq. (A7), it is apparent for cases in which the local band structure is approximately parabolic in nature (defined by an effective-mass tensor diagonal along orthogonal directions parallel and perpendicular to the band-edge \mathbf{k} point) that the Gaussian envelope functions employed above will qualitatively describe the shape of the envelope of the defect mode. In other cases this will not be true, such as that for defect perturbation with a reduced symmetry relative to the group of the wave vector, or for the localized modes formed from regions of \mathbf{k} space where the local band structure is not approximated simply by

a paraboloid. The important comparisons to numerical calculations and experimental data to be made in this paper are based upon the symmetry and dominant Fourier components of each mode, not the accuracy to which the envelope is approximated. It suffices here then to be satisfied that the IRREP classification and dominant Fourier components are correct, and remain unchanged for the ground-state envelope functions of the Appendix A.

Returning to Eq. (6) describing the localized donor modes about point a of the hexagonal lattice, we note that the $(d1, B'_1)$ donor mode transforms like a hexapole, whereas the degenerate $(d1, E_1)$ modes transform as an (x, y) -dipole pair. By introducing defect regions with lower symmetry than that of the host photonic lattice one is able to remove degeneracies in the localized mode spectrum. The X -split and Y -split cavities studied in Sec. III have a defect region with C_{2v} symmetry as opposed to the full C_{6v} symmetry of the lattice. The effects of this symmetry lowering can be simply determined using group theory by virtue of the compatibility relations between the IRREPs of the full and reduced symmetry groups:

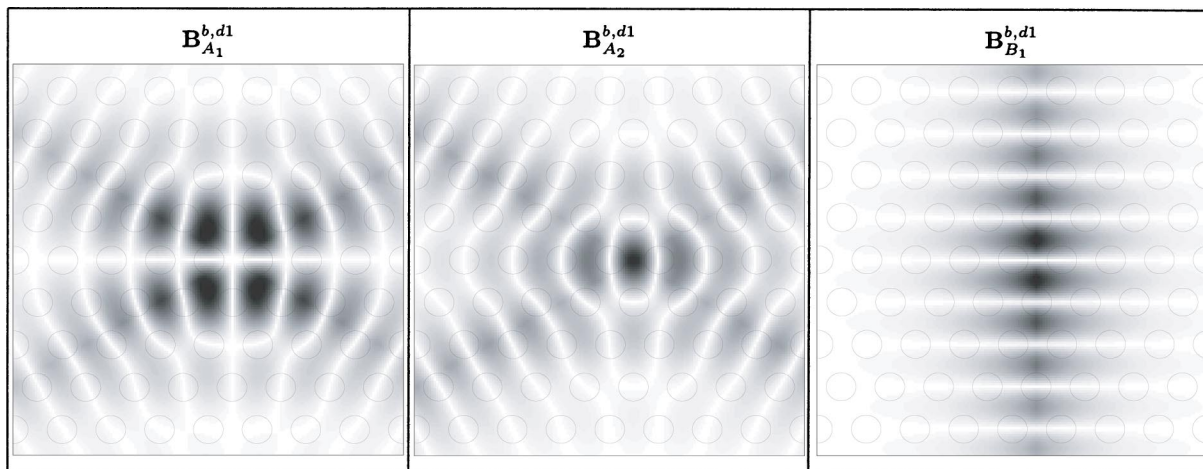


FIG. 8. Magnetic-field amplitude of the symmetry analysis conduction-band donor modes centered about point b of the hexagonal lattice.

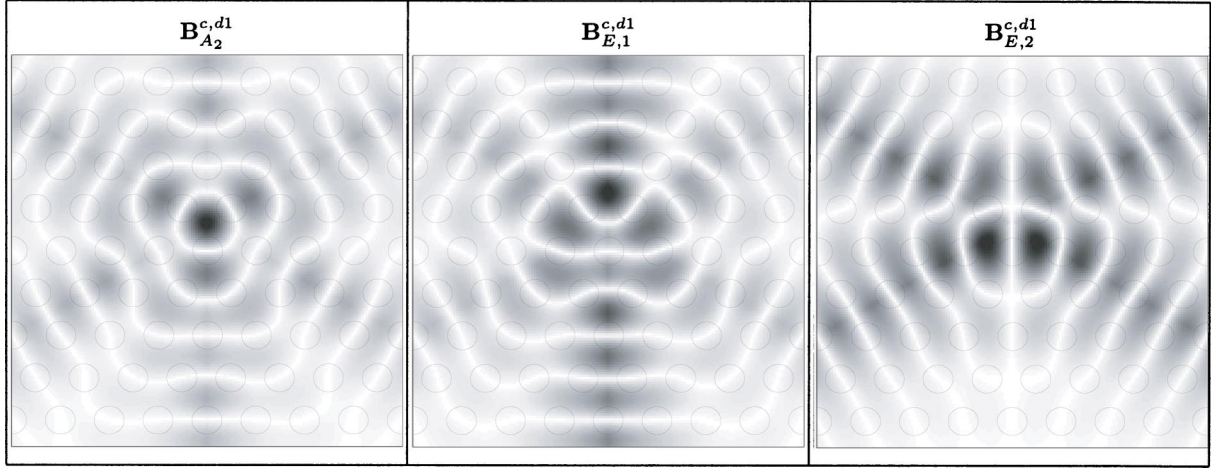


FIG. 9. Magnetic-field amplitude of the symmetry analysis conduction-band donor modes centered about point c of the hexagonal lattice.

$$\begin{aligned}
 C_{6v} &\rightarrow C_{2v}, \\
 \mathbf{B}_{B_1''}^{a,d1} &\rightarrow \mathbf{B}_{B_1}^{a,d1,1}, \\
 \mathbf{B}_{E_{1,1}}^{a,d1} &\rightarrow \mathbf{B}_{B_1}^{a,d1,2} \text{ (} x \text{ dipole)}, \\
 \mathbf{B}_{E_{1,2}}^{a,d1} &\rightarrow \mathbf{B}_{B_2}^{a,d1} \text{ (} y \text{ dipole)}. \quad (9)
 \end{aligned}$$

In the cases of the X - and Y -split cavities with C_{2v} symmetry, group theory predicts the splitting of the degenerate dipole-like modes into x - and y -dipole-like modes with differing frequencies. This is borne out both in the numerical simulations and in the experimental measurements of Sec. III below.

4. Valence-band acceptor modes

If the dielectric constant had been reduced in a small region within the photonic lattice, by enlarging an air hole, for instance, then instead of pulling the conduction-band modes down into the photonic crystal band gap the valence-band modes are “pushed” up into the band gap. In this case modes localized to the defect region are formed predominantly from

mixtures of Bloch modes from the valence-band edge. This type of defect mode is termed an acceptor mode, again in analogy to the electronic states in a crystal. For the hexagonal lattice the maximum of the valence band occurs at the J point [see Fig. 1(b)]. As in the previous section, the obvious symmetry basis to use to describe the acceptor modes is the set of degenerate valence-band modes at the J point, VB_a^J in the case of defects centered around point a , and VB_b^J and VB_c^J for defects about points b and c , respectively.

The characters of the representation $S^{a,a1}$ of VB_a^J under the C_{6v} point symmetry group, the representation $S^{b,a1}$ of VB_b^J under C_{2v} , and the representation $S^{c,a1}$ of VB_c^J under C_{3v,σ_v} are given in Table I. $S^{a,a1}$ decomposes into irreducible blocks $A_2'' \oplus B_2''$, $S^{b,a1} = A_2 \oplus B_2$, and $S^{c,a1} = E$. Using the projection operators, the basis functions VB_a^J are coupled together to form the following localized acceptor modes about point a :

$$\begin{aligned}
 \mathbf{B}_{A_2''}^{a,a1} &= \hat{z}[\cos(\mathbf{k}_{J_1} \cdot \mathbf{r}^a) + \cos(\mathbf{k}_{J_3} \cdot \mathbf{r}^a) + \cos(\mathbf{k}_{J_5} \cdot \mathbf{r}^a)], \\
 \mathbf{B}_{B_2''}^{a,a1} &= \hat{z}[\sin(\mathbf{k}_{J_1} \cdot \mathbf{r}^a) + \sin(\mathbf{k}_{J_3} \cdot \mathbf{r}^a) + \sin(\mathbf{k}_{J_5} \cdot \mathbf{r}^a)]. \quad (10)
 \end{aligned}$$

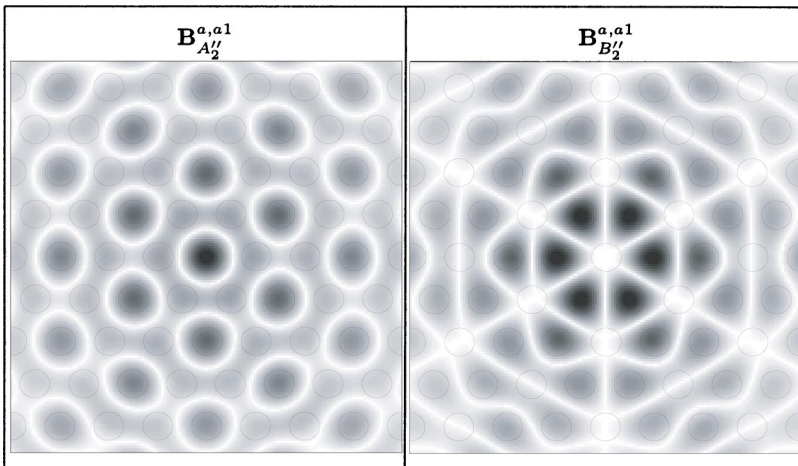


FIG. 10. Magnetic-field patterns of the symmetry analysis valence-band acceptor modes centered about point a of the hexagonal lattice.

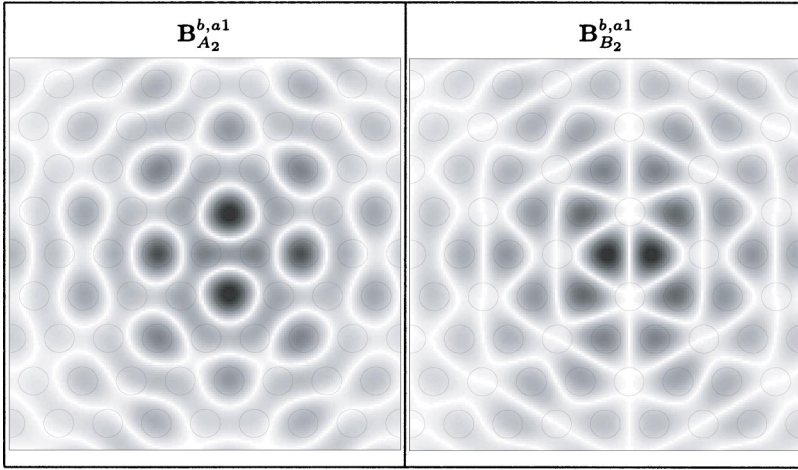


FIG. 11. Magnetic-field patterns of the symmetry analysis valence-band acceptor modes centered about point b of the hexagonal lattice.

Similarly, projecting the basis functions VB_b^J onto the IRREPs of C_{2v} and the basis functions VB_c^J onto the IRREPs of C_{3v,σ_v} , we get for the acceptor modes about point b

$$\mathbf{B}_{A_2}^{b,a1} = \hat{z}[\cos(\mathbf{k}_{J_1} \cdot \mathbf{r}^b) + \cos(\mathbf{k}_{J_3} \cdot \mathbf{r}^b) - \cos(\mathbf{k}_{J_5} \cdot \mathbf{r}^b)],$$

$$\mathbf{B}_{B_2}^{b,a1} = \hat{z}[\sin(\mathbf{k}_{J_1} \cdot \mathbf{r}^b) + \sin(\mathbf{k}_{J_3} \cdot \mathbf{r}^b) - \sin(\mathbf{k}_{J_5} \cdot \mathbf{r}^b)], \quad (11)$$

and the acceptor modes about point c

$$\mathbf{B}_{E,1}^{c,a1} = \hat{z} \left[\cos\left(\mathbf{k}_{J_1} \cdot \mathbf{r}^c + \frac{2\pi}{3}\right) + \cos\left(\mathbf{k}_{J_3} \cdot \mathbf{r}^c - \frac{2\pi}{3}\right) + \cos(\mathbf{k}_{J_5} \cdot \mathbf{r}^c) \right],$$

$$\mathbf{B}_{E,2}^{c,a1} = \hat{z} \left[\sin\left(\mathbf{k}_{J_1} \cdot \mathbf{r}^c + \frac{2\pi}{3}\right) + \sin\left(\mathbf{k}_{J_3} \cdot \mathbf{r}^c - \frac{2\pi}{3}\right) + \sin(\mathbf{k}_{J_5} \cdot \mathbf{r}^c) \right]. \quad (12)$$

Figure 10 shows plots of the \hat{z} component of the magnetic field for each of the localized acceptor modes centered about point a of the hexagonal lattice generated by the symmetry

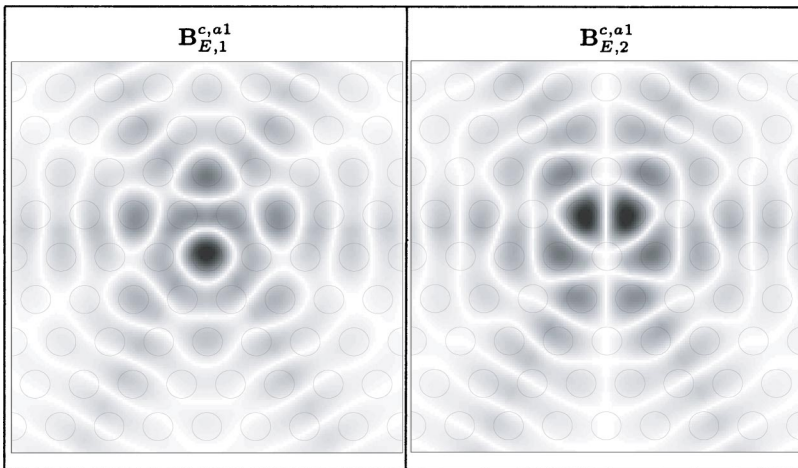


FIG. 12. Magnetic-field patterns of the symmetry analysis valence-band acceptor modes centered about point c of the hexagonal lattice.

analysis. The localized acceptor modes centered about points b and c are shown in Figs. 11 and 12.

In the X - and Y -split cavities with C_{2v} symmetry, $\mathbf{B}_{A_2''}^{a,a1}$ and $\mathbf{B}_{B_2''}^{a,a1}$ transform as A_2 and B_2 IRREPs, respectively:

$$C_{6v} \rightarrow C_{2v},$$

$$\mathbf{B}_{A_2''}^{a,a1} \rightarrow \mathbf{B}_{a,A_2}^{a1},$$

$$\mathbf{B}_{B_2''}^{a,a1} \rightarrow \mathbf{B}_{a,B_2}^{a1}. \quad (13)$$

For defect regions which strongly perturb the photonic lattice it is possible that a larger number of localized defect modes will form that can be described by the limited symmetry basis used above. This is the case for the Y -split cavity described in Sec. III, where the defect region is composed of two enlarged holes and has a relatively deep potential well for acceptor modes. As a result, in the FDTD simulations and the PL measurements of the Y -split cavity an additional shallow acceptor-type mode ($Y-A2_0$), not covered by the VB_a^J symmetry basis, is present.

In order to capture more fully the possible defect modes in a deep potential well, the symmetry basis can be expanded in a number of ways. One method would be to modulate the

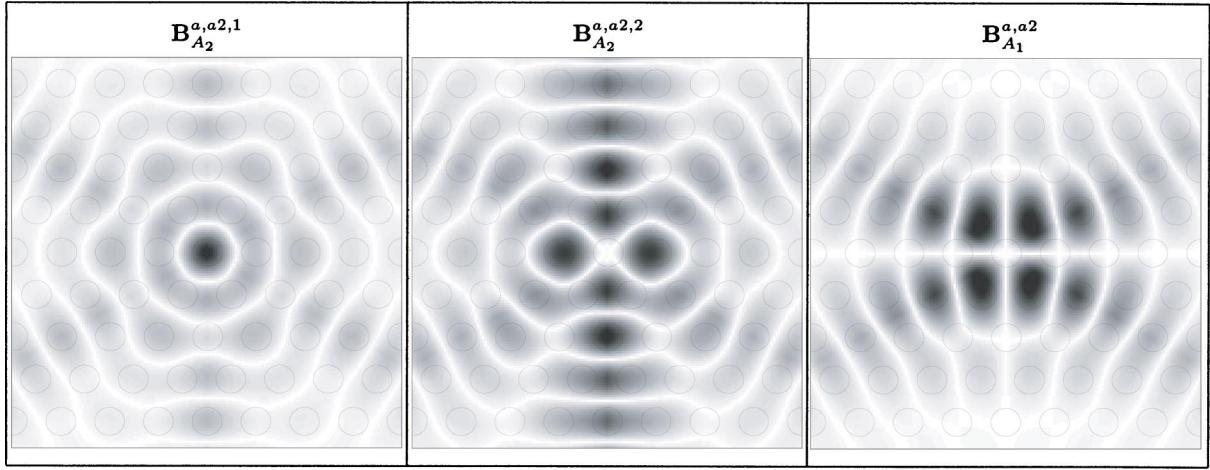


FIG. 13. Magnetic-field patterns of the symmetry analysis acceptor modes formed from the valence-band modes at the X point of the hexagonal lattice.

current symmetry basis (VB_a^J) by a set of higher-order envelope functions which contain extra nodes and antinodes. This would be more applicable in cases where there is a much greater distinction between the length scales for the defect region and the underlying lattice.²⁹ Another technique, which could be used in the case of the Y -split cavity, is to enlarge the starting symmetry basis by solving for the localized acceptor modes of each enlarged hole within the Y -split cavity separately, and then to couple the two basis sets. The symmetry basis in this case includes two copies of the acceptor modes given in Eq. (10), which are spatially separated by the distance between the two enlarged holes. This method works well for enlarged holes which are significantly displaced so as to be weakly coupled. For the closely spaced enlarged holes of the Y -split cavity it is more appropriate to treat the two enlarged holes as a single perturbation of the photonic lattice.

A third method, which will be adopted here, is based upon the observation that for defect regions which provide a deep potential well it is also possible that defect modes will form, which are composed of unperturbed photonic crystal modes located not just at the edge of the band gap, but also at other nearby (in frequency) high-symmetry k points within the IBZ. In order to represent these additional localized resonant modes the unperturbed photonic crystal modes at the additional high-symmetry k points must be included in the symmetry basis. For the hexagonal lattice the valence band at the X point is close in frequency to the band-gap edge at the J point [see Fig. 1(b)]. The symmetry basis for the X -point valence-band edge is the triply degenerate VB_a^X basis set. The representation of VB_a^X under C_{6v} , labeled $S^{a,a2}$, has the character values shown in Table I and decomposes into irreducible spaces E_2 and A_2'' . The acceptor-type modes formed from the X -point valence-band modes in a symmetric defect cavity centered about point a in the lattice are

$$\mathbf{B}_{A_2''}^{a,a2} = \hat{z}[\cos(\mathbf{k}_{X_1} \cdot \mathbf{r}^a) + \cos(\mathbf{k}_{X_2} \cdot \mathbf{r}^a) + \cos(\mathbf{k}_{X_3} \cdot \mathbf{r}^a)],$$

$$\mathbf{B}_{E_2,1}^{a,a2} = \hat{z}[2 \cos(\mathbf{k}_{X_1} \cdot \mathbf{r}^a) - \cos(\mathbf{k}_{X_2} \cdot \mathbf{r}^a) - \cos(\mathbf{k}_{X_3} \cdot \mathbf{r}^a)],$$

$$\mathbf{B}_{E_2,2}^{a,a2} = \hat{z}[\cos(\mathbf{k}_{X_2} \cdot \mathbf{r}^a) - \cos(\mathbf{k}_{X_3} \cdot \mathbf{r}^a)]. \quad (14)$$

The Y -split cavity does not have C_{6v} symmetry, but rather C_{2v} symmetry. This reduction of symmetry causes the E_2 IRREP space to split into $A_1 \oplus A_2$, and the A_2'' space to transfer over into an A_2 IRREP space:

$$C_{6v} \rightarrow C_{2v},$$

$$\mathbf{B}_{A_2''}^{a,a2} \rightarrow \mathbf{B}_{A_2}^{a,a2,1},$$

$$\mathbf{B}_{E_2,1}^{a,a2} \rightarrow \mathbf{B}_{A_2}^{a,a2,2},$$

$$\mathbf{B}_{E_2,2}^{a,a2} \rightarrow \mathbf{B}_{A_1}^{a,a2}. \quad (15)$$

Figure 13 shows the magnetic-field patterns of the acceptor modes predicted by the symmetry analysis to form out of the valence band at the X point. The shallow acceptor mode (Y - $A2_0$) found in the Y -split FDTD simulations of the next section transforms as the A_2 IRREP under C_{2v} symmetry operations. The dominant Fourier component within the FDTD-generated field pattern of Y - $A2_0$ is \mathbf{k}_{X_1} , from which we can conclude that this mode is given by $\mathbf{B}_{A_2}^{a,a2,2}$ as opposed to $\mathbf{B}_{A_2}^{a,a2,1}$.

B. Square lattice

As with the hexagonal lattice we concern ourselves here with only the fundamental even modes (TE-like) of the slab waveguide. The point-group symmetry of the square lattice photonic crystal can then be reduced to $C_{4v} = D_{4h}/\sigma_h$. A plot of the approximate in-plane band structure for the fundamental TE-like guided modes of a half-wavelength thick slab waveguide with a square array patterning of air holes is given in Fig. 14.

The high-symmetry points on the boundary or within the IBZ are [see Fig. 15(b)] the four X points [$\{\pm(1,0)k_X, \pm(0,1)k_X\}$], the four M points [$(\pm\sqrt{2}/2, \pm\sqrt{2}/2)k_M$], and the Γ -point (0,0). The first-order band edges of the square

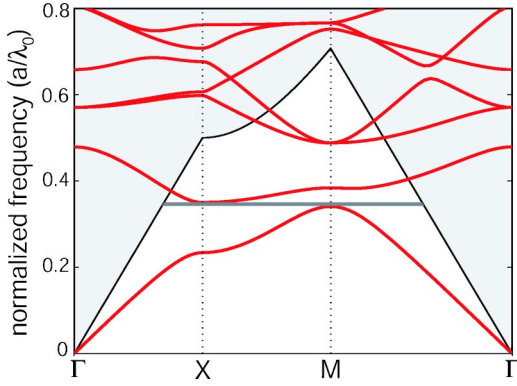


FIG. 14. Fundamental TE-like (even) guided-mode band structure ($r/a=0.35$, $n_{\text{slab}}=n_{\text{eff}}=2.65$) for a square lattice of air holes. The guided-mode band gap is seen to be much smaller for the square lattice than that in the case of the hexagonal lattice. The air (cladding) light line is shown as a solid black line.

lattice (see Fig. 14) are defined from above by the X point (“conduction”-band edge) and below by the M point (“valence”-band edge). The groups of the wave vector at the X , M , and Γ points are C_{2v} , C_{4v} , and C_{4v} , respectively. Character tables²⁸ for the two groups are given in Table II.

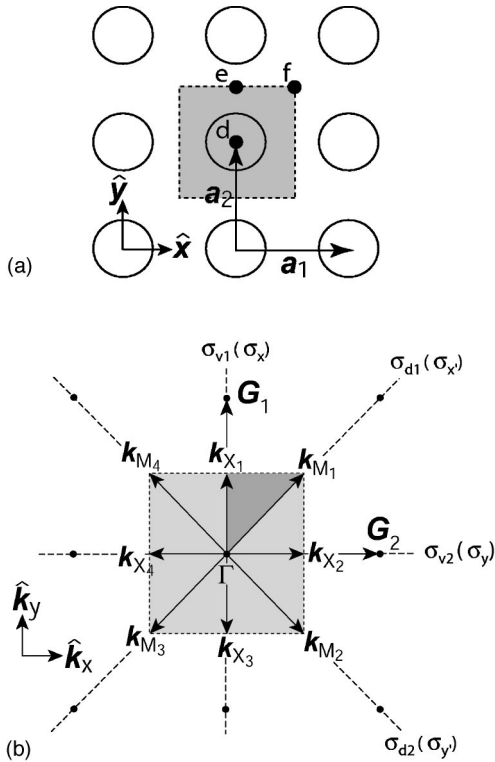


FIG. 15. Illustration of the real and reciprocal spaces of the two-dimensional PC with a square array of air holes. The high-symmetry points of the square lattice, referenced to the center of an air hole, are $\mathbf{d}=(0,0)$, $\mathbf{e}=(0,a/2)$, and $\mathbf{f}=(a/2,a/2)$. (a) Real-space lattice. $|\mathbf{a}_1|=|\mathbf{a}_2|=a$. (b) Reciprocal space. $|\mathbf{G}_1|=|\mathbf{G}_2|=2\pi/a$, $|\mathbf{k}_X|=\pi/a$, and $|\mathbf{k}_M|=\sqrt{2}\pi/a$.

TABLE II. Point-group character tables for the square lattice.

C_{4v}	E	C_2	$2C_4$	$2\sigma_v$	$2\sigma_d$
A_1''	1	1	1	1	1
A_2''	1	1	1	-1	-1
B_1''	1	1	-1	1	-1
B_2''	1	1	-1	-1	1
E	2	-2	0	0	0
S^M	4	0	0	0	-2
$S^{d,d1}$	2	-2	0	0	0
$S^{f,d1}$	2	2	0	-2	0

C_{2v,σ_d}	E	C_2	$\sigma_{x'}(\sigma_{d1})$	$\sigma_{y'}(\sigma_{d2})$
A_1'	1	1	1	1
A_2'	1	1	-1	-1
B_1'	1	-1	-1	1
B_2'	1	-1	1	-1

C_{2v,σ_v}	E	C_2	$\sigma_x(\sigma_{v1})$	$\sigma_y(\sigma_{v2})$
A_1	1	1	1	1
A_2	1	1	-1	-1
B_1	1	-1	-1	1
B_2	1	-1	1	-1
S^{X_1}	2	0	0	-2
$S^{e,d1}$	2	0	0	-2

1. X point

A symmetry basis for the modes of the square lattice PC at the X point can be found by applying the symmetry operations of the group of the wave vector ($\mathcal{G}_{o\mathbf{k}_X}=C_{2v}$) to the seed vector $\mathbf{B}_{\mathbf{k}_{X_1}}$. In this case, the basis is simply $(\mathbf{B}_{\mathbf{k}_{X_1}}, \mathbf{B}_{-\mathbf{k}_{X_1}})$. Projecting this symmetry basis onto the IR-REP spaces of C_{2v} yields

$$\mathbf{B}_{A_2}^{X_1} = \hat{z} \cos(\mathbf{k}_{X_1} \cdot \mathbf{r}),$$

$$\mathbf{B}_{B_1}^{X_1} = \hat{z} \sin(\mathbf{k}_{X_1} \cdot \mathbf{r}), \quad (16)$$

where A_2 and B_1 label the IRREP spaces of C_{2v,σ_v} (see Table II). With the origin at the center of an air hole of the lattice (point d of Fig. 15), $\mathbf{B}_{A_2}^{X_1}$ corresponds to the “valence”-band mode and $\mathbf{B}_{B_1}^{X_1}$ to the “conduction”-band mode.

In order to fully define the modes at the X point all modes of the $*\mathbf{k}$ must be included. The result is the following set of degenerate valence-band modes,

$$VB_d^X = \begin{pmatrix} v_{X_1} \\ v_{X_2} \end{pmatrix} = \hat{z} \begin{bmatrix} \cos(\mathbf{k}_{X_1} \cdot \mathbf{r}^d) \\ \cos(\mathbf{k}_{X_2} \cdot \mathbf{r}^d) \end{bmatrix}. \quad (17)$$

and degenerate conduction-band modes,

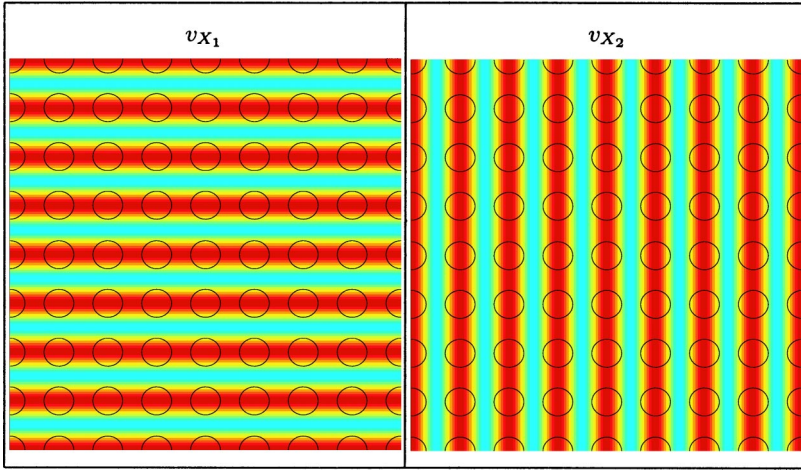


FIG. 16. Magnetic-field (amplitude) patterns of the valence-band modes of the square lattice at the X points of the IBZ generated by the symmetry basis VB_d^X .

$$CB_d^X = \begin{pmatrix} c_{X_1} \\ c_{X_2} \end{pmatrix} = \hat{z} \begin{bmatrix} \sin(\mathbf{k}_{X_1} \cdot \mathbf{r}^d) \\ \sin(\mathbf{k}_{X_2} \cdot \mathbf{r}^d) \end{bmatrix}. \quad (18)$$

The magnetic-field amplitude patterns of the approximate valence- and conduction-band modes of the square lattice at the X points of the IBZ are given in Figs. 16 and 17, respectively.

2. M point

A similar procedure may be performed in order to determine approximate forms for the TE-like valence- and conduction-band modes at the M point of the IBZ. The symmetry basis, S^M , in this case includes all the M points of the IBZ, $S^M = (\mathbf{B}_{\mathbf{k}_{M_1}}, \mathbf{B}_{\mathbf{k}_{M_2}}, \mathbf{B}_{-\mathbf{k}_{M_1}}, \mathbf{B}_{-\mathbf{k}_{M_2}})$. As determined from its character under C_{4v} (Table II), $S^M = E \oplus A_2'' \oplus B_1''$. The doubly degenerate IRREP E must represent a higher-energy-level band since the conduction- and valence-band edges are nondegenerate at the M point as shown in Fig. 14. Using only A_2'' and B_1'' , an approximate form for the valence-band-edge and conduction-band-edge modes at the M point are calculated by projecting the symmetry basis onto these IRREP spaces. With the origin centered at point d , the valence- and conduction-band-edge modes are

$$VB_d^M = (v_M) = \hat{z} [\cos(\mathbf{k}_{M_1} \cdot \mathbf{r}^d) + \cos(\mathbf{k}_{M_2} \cdot \mathbf{r}^d)] \quad (19)$$

$$CB_d^M = (c_{1M}) = \hat{z} [\cos(\mathbf{k}_{M_1} \cdot \mathbf{r}^d) - \cos(\mathbf{k}_{M_2} \cdot \mathbf{r}^d)]. \quad (20)$$

Approximate modes for the degenerate higher-frequency conduction bands represented by the IRREP E are, in one particular basis,

$$CB_d^{M,2} = \begin{pmatrix} c_{2M} \\ c_{3M} \end{pmatrix} = \hat{z} \begin{bmatrix} \sin(\mathbf{k}_{M_1} \cdot \mathbf{r}^d) - \sin(\mathbf{k}_{M_2} \cdot \mathbf{r}^d) \\ \sin(\mathbf{k}_{M_1} \cdot \mathbf{r}^d) + \sin(\mathbf{k}_{M_2} \cdot \mathbf{r}^d) \end{bmatrix}. \quad (21)$$

These higher-frequency bands will be unimportant in our present analysis where we focus on the band-edge modes defining the first-order band gap. The magnetic-field amplitude patterns of the valence- and conduction-band modes at the M point of the IBZ of the square lattice are given in Fig. 18.

In the square lattice there are three different high-symmetry points around which one may center a defect. These points are labeled d , e , and f in Fig. 15. Points d and f maintain the C_{4v} point group of the square lattice, and point e has a lowered symmetry given by the point group C_{2v, σ_v} . As was done for the hexagonal lattice, Bloch mode symmetry bases written with their origin at points d , e , or f will be

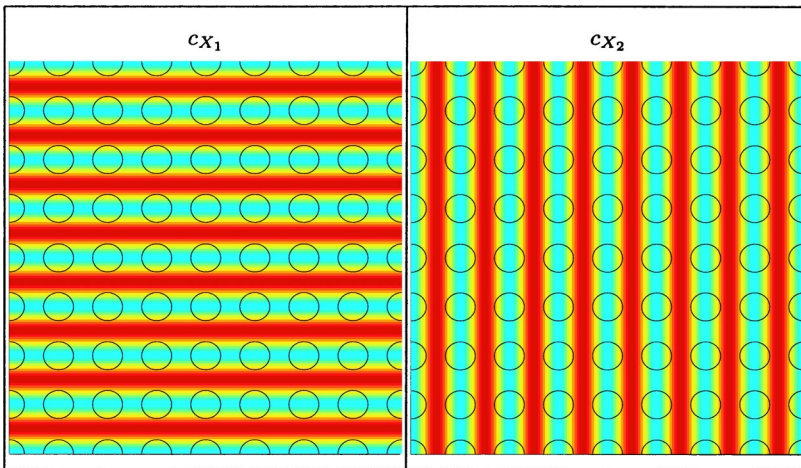


FIG. 17. Magnetic-field (amplitude) patterns of the conduction-band modes of the square lattice at the X points of the IBZ generated by the symmetry basis CB_d^X .

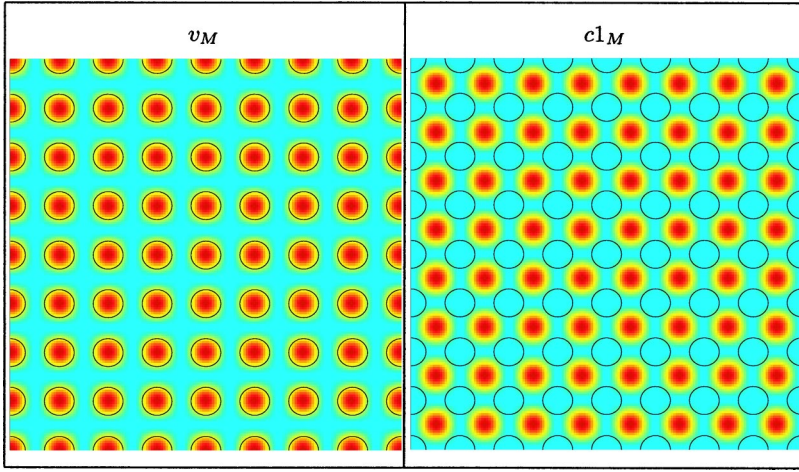


FIG. 18. Magnetic-field (amplitude) patterns of the valence- and conduction-band modes of the square lattice at the M points of the IBZ generated by the symmetry analysis (VB_d^M and CB_d^M).

indexed as such. Coordinates centered about points d , e , and f of the lattice are also labeled as \mathbf{r}^d , \mathbf{r}^e , and \mathbf{r}^f , respectively.

3. Conduction-band donor modes

For the square PC lattice the minimum in the conduction band occurs at the X point (Fig. 14). As described above, there are three different high-symmetry points within the square lattice around which defects can be created (Fig. 15). For a highly symmetric defect centered at points d and f the conduction-band-edge modes at the X point couple to form resonant modes which transform as IRREPs of C_{4v} , whereas for the lower-symmetry point e the defect modes transform as IRREPs of C_{2v,σ_v} . The representations describing the way in which the CB_d^X , CB_e^X , and CB_f^X symmetry bases transform under the appropriate point group are given by $S^{d,d1}$, $S^{e,d1}$, and $S^{f,d1}$, respectively. From their characters in Table II we find that $S^{d,d1}=E$, $S^{e,d1}=A_2 \oplus B_2$, and $S^{f,d1}=A_2'' \oplus B_2''$. Projecting the symmetry bases onto the different IRREPs gives the following conduction-band donor modes:

$$\begin{aligned} \mathbf{B}_{E,1}^{d,d1} &= \hat{z}[\sin(\mathbf{k}_{X_1} \cdot \mathbf{r}^d)], \\ \mathbf{B}_{E,2}^{d,d1} &= \hat{z}[\sin(\mathbf{k}_{X_2} \cdot \mathbf{r}^d)], \end{aligned} \quad (22)$$

centered about point d ,

$$\begin{aligned} \mathbf{B}_{A_2}^{e,d1} &= \hat{z}[\cos(\mathbf{k}_{X_1} \cdot \mathbf{r}^e)], \\ \mathbf{B}_{B_2}^{e,d1} &= \hat{z}[\sin(\mathbf{k}_{X_2} \cdot \mathbf{r}^e)], \end{aligned} \quad (23)$$

centered about point e , and

$$\begin{aligned} \mathbf{B}_{A_2''}^{f,d1} &= \hat{z}[\cos(\mathbf{k}_{X_1} \cdot \mathbf{r}^f) + \cos(\mathbf{k}_{X_2} \cdot \mathbf{r}^f)], \\ \mathbf{B}_{B_2''}^{f,d1} &= \hat{z}[\cos(\mathbf{k}_{X_1} \cdot \mathbf{r}^f) - \cos(\mathbf{k}_{X_2} \cdot \mathbf{r}^f)], \end{aligned} \quad (24)$$

centered about point f .

For the points d and f , defects may be formed with lower symmetry than that of the C_{4v} symmetry of the square lattice. We may use the compatibility relations between the IRREPs of the full and reduced symmetry groups to determine

the new mode structure. For a defect of C_{2v} symmetry with mirror planes along the \hat{x} and \hat{y} directions of Fig. 15(a) (C_{2v,σ_v}) we have the following reduction for the defect modes centered about points d and f :

$$\begin{aligned} C_{4v} &\rightarrow C_{2v,\sigma_v}, \\ \mathbf{B}_{E,1}^{d,d1} &\rightarrow \mathbf{B}_{B_1}^{d,d1} \quad (x \text{ dipole}), \\ \mathbf{B}_{E,2}^{d,d1} &\rightarrow \mathbf{B}_{B_2}^{d,d1} \quad (y \text{ dipole}), \\ \mathbf{B}_{A_2}^{f,d1} &\rightarrow \mathbf{B}_{A_2}^{f,d1,1}, \\ \mathbf{B}_{B_2}^{f,d1} &\rightarrow \mathbf{B}_{A_2}^{f,d1,2}. \end{aligned} \quad (25)$$

If instead, the defect at points d and f contain the mirror planes σ_d , the symmetry is C_{2v,σ_d} and the compatibility relations give the mode decomposition

$$\begin{aligned} C_{4v} &\rightarrow C_{2v,\sigma_d}, \\ \mathbf{B}_{E,1}^{d,d1} + \mathbf{B}_{E,2}^{d,d1} &\rightarrow \mathbf{B}_{B_1'}^{d,d1} \quad (x' \text{ dipole}), \\ \mathbf{B}_{E,1}^{d,d1} - \mathbf{B}_{E,2}^{d,d1} &\rightarrow \mathbf{B}_{B_2'}^{d,d1} \quad (y' \text{ dipole}), \\ \mathbf{B}_{A_2''}^{f,d1} &\rightarrow \mathbf{B}_{A_2'}^{f,d1}, \\ \mathbf{B}_{B_2''}^{f,d1} &\rightarrow \mathbf{B}_{A_1'}^{f,d1}. \end{aligned} \quad (26)$$

Magnetic-field patterns of the different localized donor-type defect modes formed about points d , e , and f of the square lattice are given in Fig. 19, where we have chosen to decompose the fields according to C_{2v,σ_v} .

4. Valence-band acceptor modes

For the square lattice the maximum of the valence band occurs at the M point (Fig. 14). For the square lattice the valence-band-edge modes at the M point consist of a single nondegenerate mode. This can be traced back to the fact that

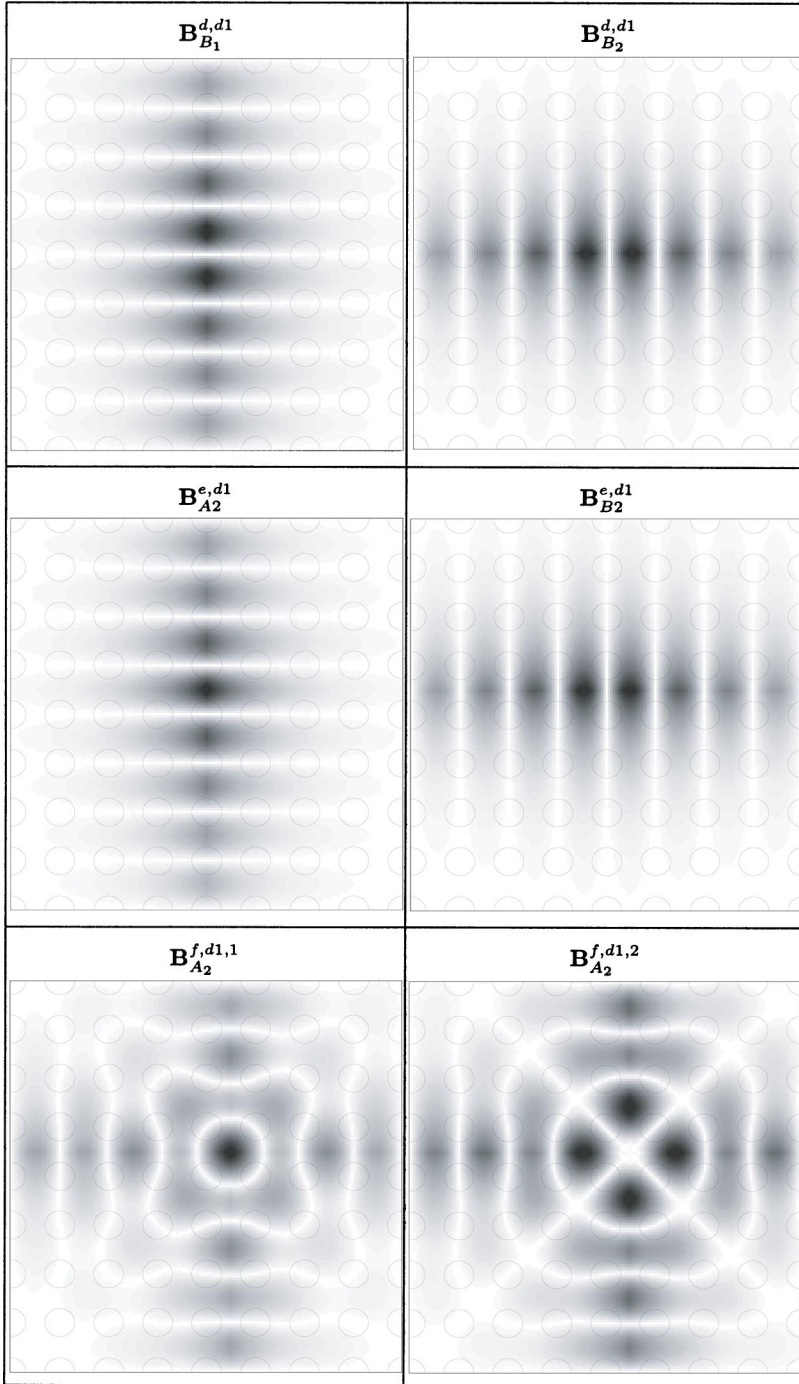


FIG. 19. Magnetic-field patterns of the localized donor modes centered about points d , e , and f of the square lattice.

the M point in the square lattice is highly symmetric, and the group of the wave vector mixes all four of the M points on the IBZ boundary. The symmetries and fundamental momentum components of the possible acceptor modes formed from the M -point band-edge modes (the approximate defect modes) are then trivially given by the single M -point valence-band-edge mode.

For the high-symmetry points d and f of the square lattice, assuming that the defect is symmetric enough so as to maintain the C_{4v} symmetry of the square lattice, the single acceptor mode is

$$\mathbf{B}_{A_2''}^{d,a1} = \hat{z}[\cos(\mathbf{k}_{M_1} \cdot \mathbf{r}^d) + \cos(\mathbf{k}_{M_2} \cdot \mathbf{r}^d)], \quad (27)$$

about point d , and

$$\mathbf{B}_{B_1''}^{f,a1} = \hat{z}[\cos(\mathbf{k}_{M_1} \cdot \mathbf{r}^f) - \cos(\mathbf{k}_{M_2} \cdot \mathbf{r}^f)], \quad (28)$$

about point f . The character of the representation S_e^{a1} of the M -point valence-band-edge mode under symmetry transformations C_{2v,σ_v} about point e is given in Table II. From its character, $S_e^{a1} = B_1$, the approximate acceptor mode of a defect centered about point e is

$$\mathbf{B}_{B_1}^{e,a1} = \hat{z}[\sin(\mathbf{k}_{M_1} \cdot \mathbf{r}^e) - \sin(\mathbf{k}_{M_2} \cdot \mathbf{r}^e)]. \quad (29)$$

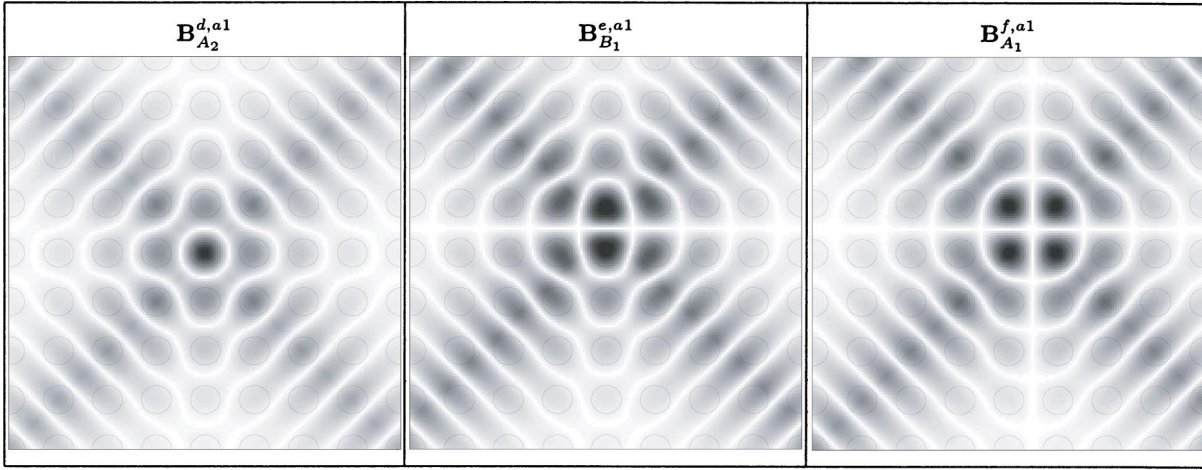


FIG. 20. Magnetic-field patterns of the acceptor-type modes formed by the valence-band M -point modes of the square lattice.

For defects of reduced symmetry about points d and f we have the following compatibility relations:

$$\begin{aligned}
 C_{4v} &\rightarrow C_{2v,\sigma_v}, \\
 \mathbf{B}_{A_2}^{d,a1} &\rightarrow \mathbf{B}_{A_2}^{d,a1}, \\
 \mathbf{B}_{B_1}^{f,a1} &\rightarrow \mathbf{B}_{A_1}^{f,a1}, \\
 C_{4v} &\rightarrow C_{2v,\sigma_d}, \\
 \mathbf{B}_{A_2}^{d,a1} &\rightarrow \mathbf{B}_{A_2}^{d,a1}, \\
 \mathbf{B}_{B_1}^{f,a1} &\rightarrow \mathbf{B}_{A_2}^{f,a1}.
 \end{aligned} \tag{30}$$

Figure 20 shows the magnetic-field patterns of the acceptor-type modes formed from the M point of the IBZ of the square lattice for defects centered about points d , e , and f . Again, as for the donor modes, the modes are shown for the C_{2v,σ_v} symmetry basis.

III. FDTD SIMULATIONS AND PHOTOLUMINESCENCE MEASUREMENTS

In order to establish the effectiveness of the above symmetry analysis of the modes of relatively localized defects within photonic crystals, we provide in this section results of numerical calculations using the FDTD method¹⁴ and PL measurements²⁶ of actual microfabricated cavities. The FDTD simulation results provide information about the resonant frequency, radiation pattern, and modal loss of PC defect cavity resonant modes, whereas the PL measurements relate both the symmetry and FDTD analyses to experimental data.

The FDTD calculations were performed on a mesh with 20 points per lattice spacing. Excitation of the cavity modes was performed by an initial field (B_z) with a localized Gaussian profile, located in a position of low symmetry so as not to exclude any possible resonant modes. The even modes of the patterned slab waveguide were selected out by using an even mirror symmetry ($\sigma_h = +1$) in the middle of the slab waveguide. In order to choose a consistent mode basis (only important for degenerate modes), as well as to reduce computation time, a pair of vertical mirror planes (σ_x, σ_y) were used to filter out cavity modes according to their pro-

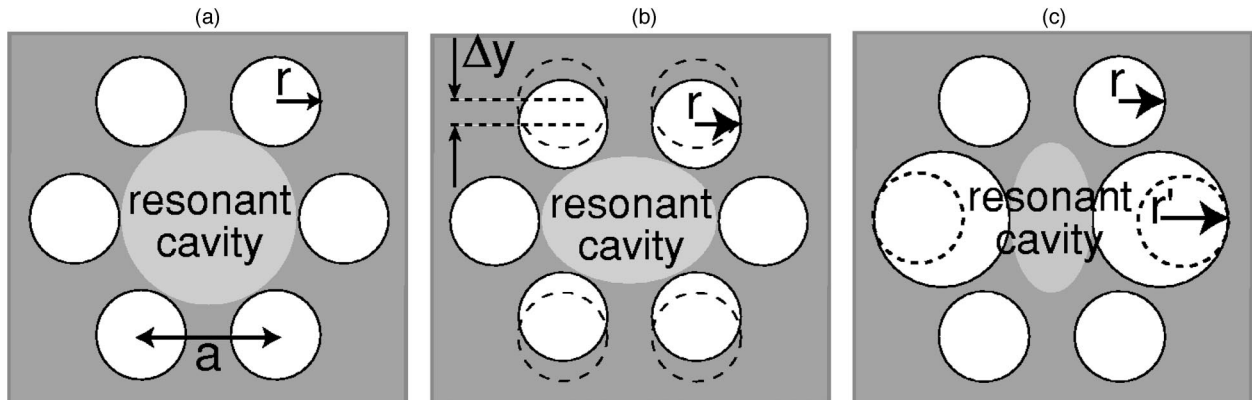


FIG. 21. PC defect cavity geometries. (a) S cavity. (b) X -split cavity. (c) Y -split cavity.

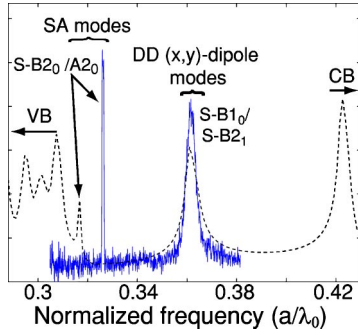


FIG. 22. FDTD and PL spectra of an S -type defect cavity with $a=515$ nm, $r/a=0.36$ nominally (graded from the center outwards, from 0.38–0.34), $n_{\text{slab}}=3.4$, and $d/a=0.409$. FDTD simulation results are shown as a dashed line.

jection on the IRREPs of C_{2v} . Each cavity mode is thus labeled by the C_{2v} IRREP by which it transforms and an index corresponding to its energy (frequency) level.

For the PL measurements the PC structures were formed in a waveguide layer containing multiple InGaAsP quantum wells which emit light in the 1500-nm wavelength band.²⁶ Optical pumping was provided by a 830-nm semiconductor laser diode, and the resulting PL was collected from a direction normal to the surface of InGaAsP sample (vertical emission from the planar defect cavities). A more detailed description of the fabrication process and measurement setup can be found in Ref. 21.

A. Symmetric (S) cavity

The simplest cavity geometry that can be readily implemented consists of a single missing hole [schematically shown in Fig. 21(a)]. We will refer to this cavity since a symmetric or S cavity as it retains the full point-group symmetry of the hexagonal lattice (C_{6v}). A FDTD simulated spectrum of a defect cavity with a central missing hole and a linear grade³⁰ in r/a (from the center outwards) of 0.38–0.34 is plotted in Fig. 22 as a dashed line. The spectrum is plotted versus normalized frequency, $\omega_n = a/\lambda_o$, where a is the lattice spacing and λ_o is the free-space wavelength. A normalized slab thickness, d/a , of 0.41 was used in the simulated structures to be consistent with the fabricated devices. To reduce computation time, the number of mirror periods (p) surrounding the central missing hole was limited to five in the simulations, save for the more extended modes for which cavities with eight periods were also simulated in order to more accurately estimate the modal losses present in the fabricated devices (see Table III).

In Fig. 22, there appear to be two distinct resonance peaks within the guided-mode band gap of the TE-like modes. Performing a mode filter¹⁴ using the C_{2v} mirror planes, we find that each resonance peak contains two different modes, yielding a total of four different localized modes whose magnetic-field patterns within the mirror-symmetry plane of the slab are shown in Table III. The two resonant modes (accidentally degenerate) associated with the peak near the valence-band edge correspond to shallow acceptor (SA) modes which transform as the A_2'' and B_2'' IRREPs of C_{6v} ,³¹ and have the same dominant in-plane Fourier components as

TABLE III. Characteristics and magnetic-field amplitude patterns of the resonant modes in a symmetric cavity with r/a linearly graded from 0.38–0.34 ($d/a=0.409$, $n_{\text{slab}}=3.4$, $p=5$).

$A_2 (-1, -1)$	$B_1 (-1, +1)$	$B_2 (+1, -1)$	
$S-A_{20}$	$S-B_{10}$	$S-B_{20}$	$S-B_{21}$
Label	Group	(σ_x, σ_y)	ω_n
$S-A_{20}$ ($\mathbf{B}_{A_2''}^{a1}$)	SA	$(-, -)$	0.320
$S-B_{10}$ ($\mathbf{B}_{B_1}^{d1,1}$)	DD	dipole (x)	0.361
$S-B_{20}$ ($\mathbf{B}_{B_2''}^{a1}$)	SA	$(+, -)$	0.322
$S-B_{21}$ ($\mathbf{B}_{B_1}^{d1,2}$)	DD	dipole (y)	0.360

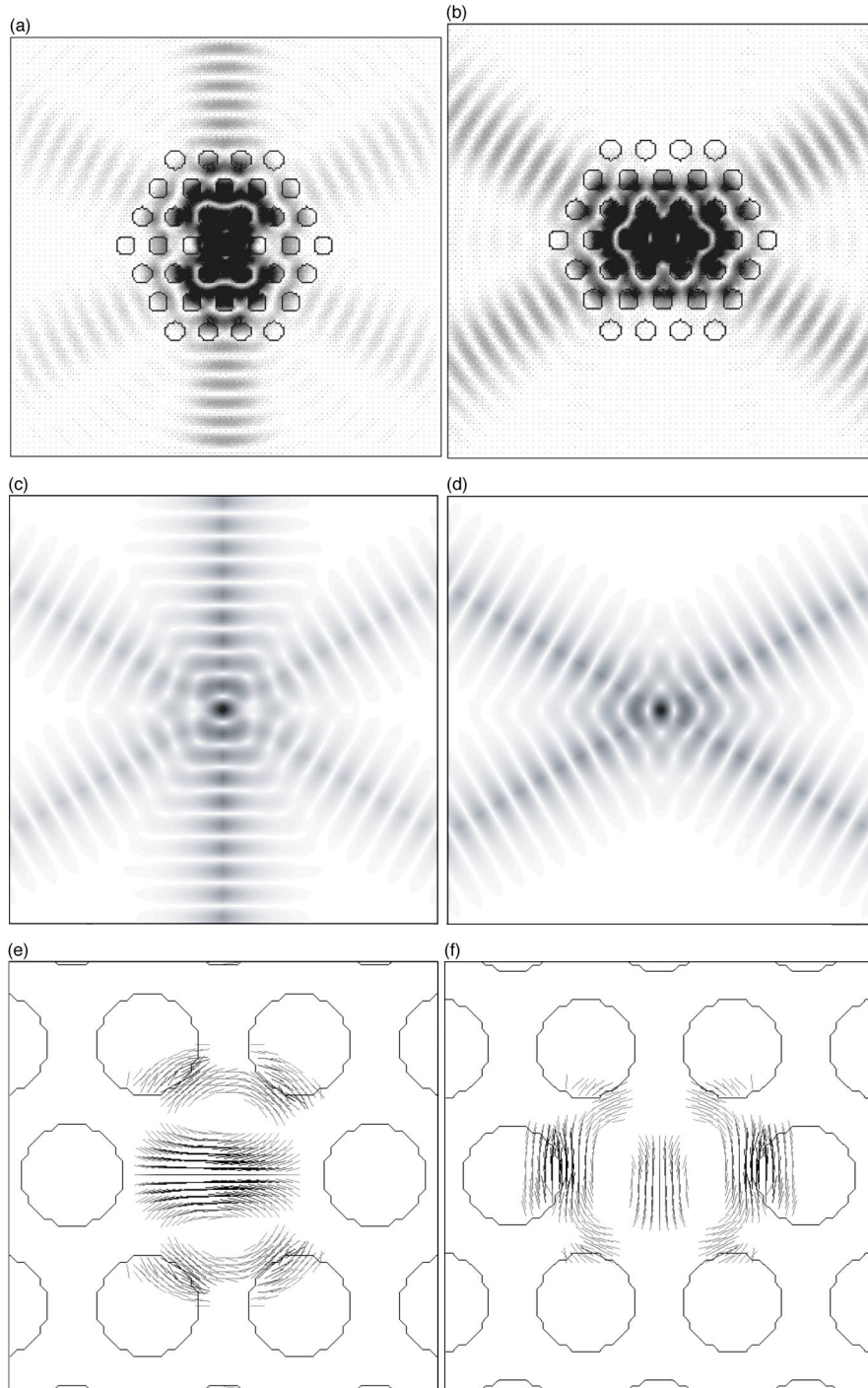


FIG. 23. (a) In-plane x -dipole mode radiation pattern. (b) In-plane y -dipole mode radiation pattern. (c) Symmetry analysis x -dipole mode. (d) Symmetry analysis y -dipole mode. (e) x -dipole vector plot. (f) y -dipole vector plot. In-plane radiation losses (electric-field amplitude saturated) of the x - and y -dipole modes (degenerate case) are shown in (a) and (b), respectively. The electric-field amplitudes of the corresponding defect modes generated by the symmetry analysis are shown in (c) and (d) for comparison. In (e) and (f) the vector plots of the electric field of the (x,y) -dipole modes in the middle of the slab waveguide are shown.

$\mathbf{B}_{A_2'}^{a1}$ and $\mathbf{B}_{B_2'}^{a1}$ of the symmetry analysis in Sec. II. The addition of these SA modes is a result of the linear grading in hole radius, which forms a potential well for acceptor-type modes. Of particular interest are the strongly localized pair of degenerate deep donor (DD) dipolelike modes near the center of the band gap. From the plots of the electric-field

intensity of the x - and y -dipole modes shown in Figs. 23(a) and 23(b), we see that the fundamental \mathbf{k} components of the x - and y -dipole-like modes correspond nicely with the approximate field patterns predicted by the symmetry analysis. $\mathbf{B}_{E_{1,1}}^{d1}$ represents the x -dipole mode and $\mathbf{B}_{E_{1,2}}^{d1}$ the y -dipole mode. Even the subtle difference in the in-plane radiation

pattern of the (x,y) -dipole modes as calculated numerically using FDTD is contained within the symmetry analysis as can be seen by the lack of a third standing-wave component in the y -dipole ($\mathbf{B}_{E_{1,2}}^{d1}$) mode.

A PL spectrum from a S defect cavity with $a=515$ nm, $r/a \approx 0.36$, and $d/a=0.41$ is shown overlaid upon the FDTD simulation in Fig. 22. The emission from the S cavity also shows the presence of two dominant peaks, one very close to the DD peak and one close to the SA peak. Owing to the small scale of the photonic crystal defect cavities, the field patterns of the deep donor modes strongly resemble that of an oscillating electric dipole. A vector plot of the \mathbf{E} field of the x - and y -dipole modes in the plane of the slab is shown in Figs. 23(c) and 23(d). Polarization measurements of the DD peak³² confirm that the emission is polarized predominantly along two orthogonal directions consistent with the x - and y -dipole directions. The experimental determination of the absolute frequency of the DD dipole modes provides a reference point from which to classify the rest of the cavity modes, and also provides a measure of the accuracy of the FDTD calculations.

A list of properties of the two SA and two DD localized defect modes are given in Table III. The numerically calculated losses of each cavity mode are represented by effective in-plane and out-of-plane quality factors,¹⁴ Q_{\parallel} and Q_{\perp} , respectively. The effective mode volume, V_{eff} , is calculated from an estimate of the full width at half maximum value of the electric-field energy density in each direction,³³ and is given in units of cubic half wavelengths. As a result of the large porosity of the PC obtained during the fabrication process,²⁶ FDTD simulations predict a rather large vertical diffraction loss (small Q_{\perp}) for the highly localized dipolelike modes. In contrast, the unintentionally introduced linear grade in hole radius provides sufficient in-plane localization to produce high- Q SA modes. For the fabricated defect cavities with eight periods of the photonic crystal mirror ($p=8$), the quality factor for the S - $B2_0$ mode is theoretically estimated to be as high as 7500, limited by radiative losses in the plane of the photonic lattice. It is for this reason that room-temperature lasing in S defect cavities is limited to the SA mode peak,²¹ and reduced temperatures are required in order for the DD dipolelike modes to lase (see Sec. III C).

B. X split (X) cavity

Another type of defect cavity that was fabricated and tested, referred to as the X -split cavity, is shown in Fig. 21(b). In this cavity the four air holes on the top and bottom of the central missing hole are moved inwards a distance Δy , reducing the defect symmetry from C_{6v} to C_{2v} . In the fabricated structures $\Delta y \sim 0.05a \sim 25$ nm. A FDTD spectrum of an X -split cavity with Δy matching that of the fabricated devices is plotted in Fig. 24. The magnetic-field amplitudes of the different resonant modes found in the FDTD spectrum are shown in Table IV. The deep donor (x,y) -dipole modes are seen to split, as expected from the symmetry analysis of the previous section, with the x dipole being higher in frequency. The geometry of the cavity also introduces two shallow acceptor modes, X - $A2_0$ and X - $B2_0$. These are the same

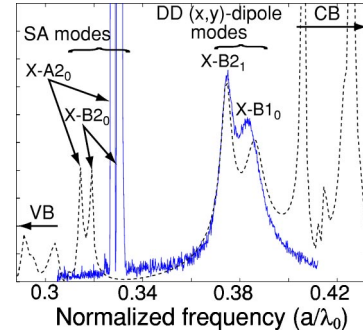


FIG. 24. PL and FDTD spectra showing the resonant modes of an X -split defect cavity with $r/a=0.38-0.34$, $d/a=0.409$, $n_{\text{slab}}=3.4$, and $\Delta y=0.05a$. FDTD simulation results are shown as a dashed line.

modes as those found in the S cavity, in which the linear grade in hole size created a potential well for additional acceptor-type modes. As such, these modes have the same dominant in-plane Fourier components as $\mathbf{B}_{A_2}^{a1}$ and $\mathbf{B}_{B_2}^{a1}$ of Sec. II.

Figure 24 also contains a PL spectrum for an X -split cavity ($r/a=0.38-0.34$, $d/a=0.409$, $\Delta y=0.05a$) overlaid upon the FDTD spectrum. The PL spectrum shows the presence of two pairs of resonance peaks. The SA and DD peaks of the S cavity have each split into two distinct resonances. The positions of these peaks correspond well with those of the FDTD simulation, and allow for their identification (see Table IV) using the nomenclature developed in Sec. II. This classification is further supported by polarization measurements of the DD modes.³² These measurements show that the two modes are highly polarized along orthogonal directions, with the longer-wavelength peak identified as the y -dipole mode and the shorter wavelength peak as the x -dipole mode.

FDTD calculated properties of the SA and DD resonant modes of the X -split cavity are listed in Table IV. As in the S cavity the DD dipolelike modes are seen to be highly localized; however, the vertical diffraction loss suffered by the dipolelike modes is much more severe in the case of the X -split cavity, especially so for the x -dipole mode. This can be seen in the PL spectrum of the X -split cavity in which the higher-frequency DD peak is significantly broader than its lower-frequency partner. Room-temperature lasing (pulsed) was limited to the X - $A2_0$ and X - $B2_0$ SA modes. Measurements of the threshold pump power of each SA mode from a large array of devices showed a consistently lower threshold value for the higher-frequency X - $B2_0$ mode,²¹ in agreement with its higher estimated Q value given in Table IV.

C. Y-split (Y) cavity

In the Y -split cavity, illustrated in Fig. 21(c), the nearest-neighbor holes on both sides of the central missing hole along the ΓJ direction are enlarged and moved slightly inwards. The degree of splitting is measured by r'/r , the scaling factor of the enlarged holes. The cavities studied here use hole enlargements which result in a much stronger perturbation of the cavity than in the X -split case. A FDTD simula-

TABLE IV. Characteristics and magnetic-field (amplitude) patterns of the resonant modes in an X -split cavity ($r/a=0.38-0.34, d/a=0.409, n_{\text{slab}}=3.4, \Delta y=0.05a, p=5$).

$A2 (-, -)$		$B1 (-, +)$		$B2 (+, -)$			
$X-A2_0$		$X-B1_0$		$X-B2_0$		$X-B2_1$	
Label	Group	(σ_x, σ_y)		ω_n			
$X-A2_0$ ($\mathbf{B}_{A_2}^{a1}$)	SA	$(-, -)$		0.316			
$X-B1_0$ ($\mathbf{B}_{B_1}^{d1,2}$)	DD	dipole (x)		0.385			
$X-B2_0$ ($\mathbf{B}_{B_2}^{a1}$)	SA	$(+, -)$		0.319			
$X-B2_1$ ($\mathbf{B}_{B_2}^{d1}$)	DD	dipole (y)		0.374			

tion showing the mode spectrum of a Y -split cavity with the two nearest-neighbor holes enlarged by $r'/r=1.5$ is shown in Fig. 25. The magnetic-field amplitudes of the various localized defect modes of the Y -split cavity are given in Table V. There are now at least four different localized modes within the photonic band gap. The two enlarged holes act as centers for acceptor modes and give rise to two deep acceptor (DA) modes in the spectrum. These DA modes are labeled as $Y-A2_1$ and $Y-B2_0$, and correspond to the SA modes of the S and X -split cavities. The strength of the perturbation to the photonic lattice produces an additional SA mode as well. As noted in Sec. II, this mode has the same dominant in-plane Fourier components as $\mathbf{B}_{A_2}^{a2,2}$ of the symmetry analysis. We further note that the splitting of the (x,y) -dipole

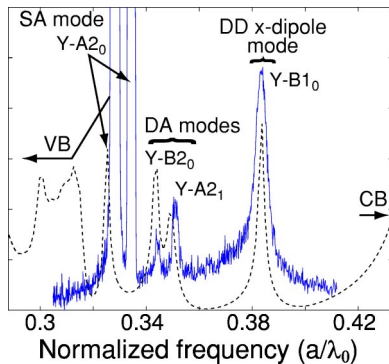


FIG. 25. PL and FDTD spectra of the resonant modes in a Y -split defect cavity with $r/a=0.38-0.34, r'/a=0.51, d/a=0.409$, and $n_{\text{slab}}=3.4$. FDTD simulation results are shown as a dashed line.

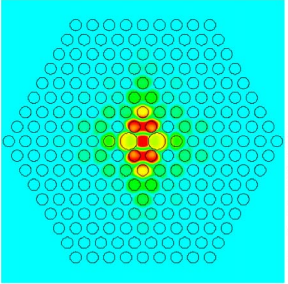
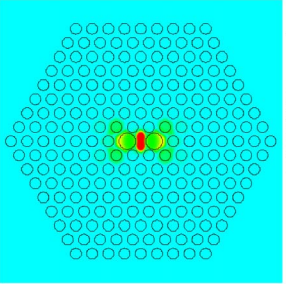
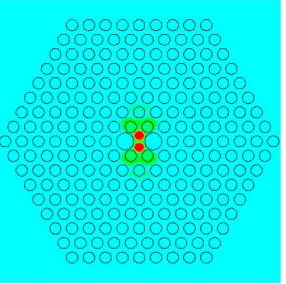
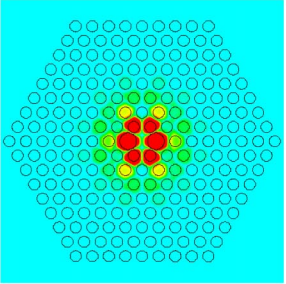
modes is so strong in this case that the y -dipole mode is completely pushed out of the band gap and only the x -dipole mode remains.

The PL spectrum for a Y -split cavity ($r/a=0.38-0.34, r'/a=0.51, d/a=0.409$), shown along with the FDTD spectrum in Fig. 25, confirms many of the predictions made by the group-theory and FDTD analyses. In particular, we note the presence of a SA peak, two DA peaks, and a single DD peak. Polarization measurements of this DD mode³² show it to be strongly polarized in a direction corresponding to the x -dipole mode. Table V also contains a list of the FDTD calculated properties of the Y -split cavity defect modes. It is interesting to note that the DA modes are as well localized as the DD dipolelike mode. The low- Q values of the DA modes and the x -dipole mode are due to the large size of the splitting holes. Room-temperature (pulsed) lasing was observed from all but the DD x -dipole mode in the Y -split cavities.²¹ At reduced temperatures ($T < 150$ K), it was possible to obtain pulsed lasing action of the x -dipole mode.¹⁶ Since the DA modes have similar Q values to that of the x -dipole mode, it is suspected that the difficulty in obtaining lasing from the DD mode may have more to do with the misalignment of the gain spectrum with the resonance wavelength of the defect cavities fabricated and tested in this experiment than with the modal loss.

IV. SUMMARY

The resonant modes of localized defects in hexagonal and square 2D photonic lattices have been examined analytically through group-theoretical methods. Although the method is

TABLE V. Characteristics and magnetic-field (amplitude) patterns of the resonant modes in a Y -split cavity ($r/a=0.38-0.34, r'/a=0.51, d/a=0.409, n_{\text{slab}}=3.4, p=8$).

A2 $(-, -)$		B1 $(-, +)$	B2 $(+, -)$
$Y-A2_0$	$Y-A2_1$	$Y-B1_0$	$Y-B2_0$
			
Label	Group	(σ_x, σ_y)	ω_n
$Y-A2_0$ ($\mathbf{B}_{A_2}^{a2,2}$)	SA	$(-, -)$	0.326
$Y-A2_1$ ($\mathbf{B}_{A_2}^{a1}$)	DA	$(-, -)$	0.350
$Y-B1_0$ ($\mathbf{B}_{B_1}^{d1,2}$)	DD	dipole (x)	0.384
$Y-B2_0$ ($\mathbf{B}_{B_2}^{a1}$)	DA	$(+, -)$	0.344

general, the focus in this paper has been on the TE-like fundamental even modes present in optically thin patterned dielectric slab waveguides. Approximate mode patterns for those localized states formed within the lowest-frequency gap are determined for defects oriented around the high-symmetry points of the square and hexagonal lattices. Numerical calculations using the FDTD method, along with PL spectroscopy of microfabricated devices in InP, are presented for defects of varying symmetry within the hexagonal lattice structure. The simple group-theory analysis is seen to describe the approximate behavior of the localized resonant modes in such devices, predicting not only the correct symmetry of the modes but many of their subtle features. Experimental characterization of fabricated structures largely confirms the accuracy of both FDTD and symmetry models. The closeness of the correspondence illustrates the degree to which the emission properties of resonant modes of localized defects within photonic crystals can be *specified* by utilizing a combination of the numerical and symmetry-based techniques described in this paper.

ACKNOWLEDGMENTS

The authors would like to thank A. Scherer for help with device processing, as well as J. D. O'Brien and P. D. Dapkus for the growth of the InGaAsP material used to create the PC cavities. K. Srinivasan thanks the Hertz Foundation for its financial support.

APPENDIX: SYMMETRY OF THE ENVELOPE

Implicit in the derivation of the symmetries and dominant Fourier components of the defect states described in Sec. II

were the transformation properties of the envelope functions describing the localization of each mode. In those sections it was assumed that the envelope functions transformed as the identity under all point symmetry operations of the defect system. In this Appendix we utilize a Wannier-like equation for localized photon states to study the transformation properties of the ground-state envelope functions. Since the defect modes studied in the previous sections were fundamental TE-like modes of a symmetric slab PC, we use here a scalar field theory in terms of the component of the magnetic field normal to the slab.

In forming a defect state by perturbing the lattice in a localized region of space, the Bloch modes in proximity to the degenerate satellite extrema of a band edge, the $\{\mathbf{k}_i; i=1, 2, \dots, M\}$ points of the $^*\mathbf{k}$ (from here on reference to the $^*\mathbf{k}$ refers implicitly to the orbit of this band edge), are most strongly coupled together:³⁴

$$H_d(\mathbf{r}) = \sum_i c_i \sum_{\mathbf{k}} \tilde{\Gamma}_i(\mathbf{k} - \mathbf{k}_i) \frac{1}{L} h_{l,\mathbf{k}} e^{i\mathbf{k} \cdot \mathbf{r}}, \quad (\text{A1})$$

where $H_d(\mathbf{r})$ is the localized defect state, l labels the band index, and \mathbf{k} labels the in-plane crystal momentum. The Bloch waves of the unperturbed 2D lattice, $H_{l,\mathbf{k}}$, are written as

$$H_{l,\mathbf{k}} = \frac{1}{L} h_{l,\mathbf{k}}(\mathbf{r}) e^{i\mathbf{k} \cdot \mathbf{r}}, \quad (\text{A2})$$

with L^2 equal to the area of the 2D photonic crystal and the set of periodic functions, $h_{l,\mathbf{k}}(\mathbf{r})$, at crystal momentum \mathbf{k} ,

satisfying their own set of orthogonality relations (normalized over the lattice unit cell v),

$$\langle h_{l',\mathbf{k}} | h_{l,\mathbf{k}} \rangle_v \equiv \frac{1}{v} \int_v d^2r h_{l',\mathbf{k}}^* h_{l,\mathbf{k}} = \delta_{l',l}. \quad (\text{A3})$$

The $\tilde{\Gamma}_i$ are a set of Fourier space envelope functions, which in the spirit of effective-mass theory have amplitudes localized around $\mathbf{k} = \mathbf{k}_i$. Note that throughout this analysis the band of interest at the band edge is considered to be nondegenerate and we neglect *interband* mixing.³⁴

Assuming that $h_{l,\mathbf{k}}$ do not vary significantly (using a similar argument as in Ref. 35) over the range of each Fourier space envelope function,

$$H_d(\mathbf{r}) \approx \sum_i c_i \frac{1}{L} h_{l,\mathbf{k}_i} e^{i\mathbf{k}_i \cdot \mathbf{r}} \left[\sum_{\Delta\mathbf{k}} \tilde{\Gamma}_i(\Delta\mathbf{k}) e^{i\Delta\mathbf{k} \cdot \mathbf{r}} \right], \quad (\text{A4})$$

where $\Delta\mathbf{k} \equiv \mathbf{k} - \mathbf{k}_i$. Writing the envelope functions in real space

$$\Gamma_i(\mathbf{r}) = \sum_{\Delta\mathbf{k}} \tilde{\Gamma}_i(\Delta\mathbf{k}) e^{i\Delta\mathbf{k} \cdot \mathbf{r}} \quad (\text{A5})$$

allows us to rewrite Eq. (A4) as

$$H_d(\mathbf{r}) \approx \sum_i c_i \frac{1}{L} h_{l,\mathbf{k}_i} e^{i\mathbf{k}_i \cdot \mathbf{r}} \Gamma_i(\mathbf{r}). \quad (\text{A6})$$

It is in this way that the real-space envelope of localized defect modes can be interpreted in the Fourier domain³⁵ as a result of the *intra*band mixing of the unperturbed Bloch modes of the crystal. As will be presented elsewhere,³⁶ one can derive a Wannier-like equation for the envelope of localized defect states within PC slab waveguides. The resulting eigenvalue equation for the magnetic-field envelope about each element of the $^*\mathbf{k}$, where the mixing of Bloch states between different satellite points of the $^*\mathbf{k}$ are neglected, is given by

$$\{[\Delta\lambda_d - \lambda'_{l,i}(\hbar^{-1}\hat{\mathbf{p}})] - \Delta\eta'_{l,i}(\mathbf{r})\} \Gamma_i(\mathbf{r}) = 0, \quad (\text{A7})$$

with effective potential

$$\begin{aligned} \Delta\eta'_{l,j}(\mathbf{r}) = & \Delta\eta(\mathbf{r}) K_{l,l}(\mathbf{k}_i, \mathbf{k}_j, \mathbf{G}_{j,i}) \\ & + \nabla[\Delta\eta(\mathbf{r})] \cdot \mathbf{L}_{l,l}(\mathbf{k}_i, \mathbf{k}_j, \mathbf{G}_{j,i}). \end{aligned} \quad (\text{A8})$$

In the above set of equations $\Delta\lambda_d = \lambda_d - \lambda_{l,o}$ is the eigenvalue referenced to the top (bottom) of the band edge, $\Delta\mathbf{k}_{j,i} \equiv \mathbf{k}_j - \mathbf{k}_i$, $\hat{\mathbf{p}} = -i\hbar\nabla$ as in quantum mechanics, and $\Delta\eta(\mathbf{r})$ is the local perturbation to the inverse of the dielectric constant of the PC. The local band structure of the l th band in a neighborhood of each element of $^*\mathbf{k}$ is given by $\lambda'_{l,\mathbf{k}}$

$$\lambda_{l,\mathbf{k}'} \approx [\lambda_{l,o} + \lambda'_{l,i}(\Delta\mathbf{k})] + O(\Delta\mathbf{k}^3), \quad (\text{A9})$$

where $\lambda_{l,o}$ is the top (bottom) of the band edge, $\Delta\mathbf{k} = \mathbf{k}' - \mathbf{k}_i$, and where we take $\lambda'_{l,i}$ to contain only terms up to second order in elements of $\Delta\mathbf{k}$.³⁴ The scalar and vector

coupling matrix elements are determined from the Bloch modes of the unperturbed lattice to be

$$\begin{aligned} K_{l',l}(\mathbf{k}', \mathbf{k}, \mathbf{G}) = & -\frac{1}{v} \int_v d^2r e^{i\mathbf{G} \cdot \mathbf{r}} h_{l',\mathbf{k}'}^* \\ & \times (\nabla^2 + 2i\mathbf{k} \cdot \nabla - |\mathbf{k}|^2) h_{l,\mathbf{k}}, \end{aligned} \quad (\text{A10})$$

$$\mathbf{L}_{l',l}(\mathbf{k}', \mathbf{k}, \mathbf{G}) = -\frac{1}{v} \int_v d^2r e^{i\mathbf{G} \cdot \mathbf{r}} h_{l',\mathbf{k}'}^* (\nabla + i\mathbf{k}) h_{l,\mathbf{k}}, \quad (\text{A11})$$

where \mathbf{G} are reciprocal-lattice vectors, and $\mathbf{G}_{i,i} = \mathbf{0}$.

In considering the mixing of states from a symmetry standpoint it is necessary to know how the envelope functions transform under the point-group symmetry operations of the defect. Of most importance here are the ground-state envelope functions. As discussed in more detail in Sec. II A, this is due to the relatively localized nature of the defect regions present in the devices designed and tested in Sec. III. For delocalized defect regions extending over many lattice periods a more extensive set of envelope functions, including higher-order functions with added nodes and antinodes must be included. The choice of such a set of envelope functions will depend on the geometry of the boundary of the defect.³⁷ For the present work, we choose only the ground-state envelope functions $\Gamma_i(\mathbf{r}) = \Gamma_{i,o}(\mathbf{r})$.

The ground state of a system is in general invariant under the symmetries of the Hamiltonian of that system.^{38,39} Thus, the ground-state envelope function should transform as the identity of the point symmetry group of the Wannier-like equation given in Eq. (A7). The spatial symmetries of Eq. (A7) are those of $\lambda'_{l,i}(\hbar^{-1}\hat{\mathbf{p}})$ and $\Delta\eta'_{l,i}(\mathbf{r})$. Since $\hat{\mathbf{p}} = -i\hbar\nabla$ transforms as a wave vector under rotary reflections, the transformation properties of $\lambda'_{l,i}(\hbar^{-1}\hat{\mathbf{p}})$ are equivalent to those of $\lambda'_{l,i}(\Delta\mathbf{k})$, which as mentioned earlier is a local expansion of $\lambda_l(\mathbf{k})$ in a neighborhood of \mathbf{k}_i . The limited local correspondence between $\lambda'_{l,i}$ and λ_l results in a reduced symmetry of $\lambda'_{l,i}$ from that of λ_l .

In order to determine the symmetry of $\lambda'_{l,i}$ we decompose the point-group operations of the crystal, \mathcal{G} , into the group of the wave vector $\mathcal{G}_{\mathbf{k}_i}$ and a set of coset generators $\{d_{ij}; j = 1, \dots, M\}$: $\mathcal{G} = \sum_j d_{ij} \mathcal{G}_{\mathbf{k}_i}$, where M is the number of elements of the $^*\mathbf{k}$ and the d_{ij} take \mathbf{k}_i to \mathbf{k}_j . $\lambda_l(\mathbf{k})$ is invariant under all the operations of \mathcal{G} . $\lambda'_{l,i}(\Delta\mathbf{k})$ on the other hand can at most be invariant under the operations of $\mathcal{G}_{\mathbf{k}_i}$, which are those operations of \mathcal{G} that take a neighborhood of \mathbf{k}_i into itself modulo a reciprocal-lattice vector. That $\lambda'_{l,i}(\Delta\mathbf{k})$ is in fact invariant under *all* such operations follows by considering the operation of an element of $\mathcal{G}_{\mathbf{k}_i}$ acting upon $\lambda_l(\mathbf{k})$ with $\mathbf{k} = \Delta\mathbf{k} + \mathbf{k}_i$:

$$\{\mathcal{G}_{\mathbf{k}_i}\} \lambda_l(\mathbf{k}) = \lambda_l(\{\mathcal{G}_{\mathbf{k}_i}\} \mathbf{k}) = \lambda_l[\{\mathcal{G}_{\mathbf{k}_i}\} \Delta\mathbf{k} + (\mathbf{k}_i + \mathbf{G})]. \quad (\text{A12})$$

Since the dispersion relation is periodic in reciprocal space, $\lambda_l[\{\mathcal{G}_{\mathbf{k}_i}\} \Delta\mathbf{k} + (\mathbf{k}_i + \mathbf{G})] = \lambda_l(\{\mathcal{G}_{\mathbf{k}_i}\} \Delta\mathbf{k} + \mathbf{k}_i)$, which gives

$$\lambda_l(\Delta\mathbf{k} + \mathbf{k}_i) = \{\mathcal{G}_{\mathbf{k}_i}\} \lambda_l(\Delta\mathbf{k} + \mathbf{k}_i) = \lambda_l(\{\mathcal{G}_{\mathbf{k}_i}\} \Delta\mathbf{k} + \mathbf{k}_i). \quad (\text{A13})$$

This then implies that $\lambda'_{l,i}$ is invariant under all the operations of $\mathcal{G}_{\mathbf{k}_i}$, $\lambda'_{l,i}(\{\mathcal{G}_{\mathbf{k}_i}\} \Delta\mathbf{k}) = \lambda'_{l,i}(\Delta\mathbf{k})$. The other operations of \mathcal{G} which take \mathbf{k}_i into \mathbf{k}_j , $j \neq i$, simply transform $\lambda'_{l,i}$ into $\lambda'_{l,j}$. In situations where the crystal lacks inversion symmetry (the lattice itself always has inversion symmetry) the effects of time-reversal symmetry must be considered. If there exists a reciprocal-lattice vector \mathbf{G} that connects \mathbf{k}_i and $-\mathbf{k}_i$, and time-reversal symmetry does not mix the l th band with another band,⁴⁰ then $\lambda'_{l,i}(\Delta\mathbf{k}) = \lambda'_{l,i}(-\Delta\mathbf{k})$ regardless of the lack of crystal symmetry. In this case, with the inclusion of time-reversal symmetry, the full symmetry of $\lambda'_{l,i}$ is given by the point group formed from the elements of $\mathcal{G}_{\mathbf{k}_i} \cup \{\hat{I}\}$, where \hat{I} is the inversion operator. We will use $\mathcal{G}'_{\mathbf{k}_i}$ to label the point group which is equivalent to $\mathcal{G}_{\mathbf{k}_i}$ except in those situations where time-reversal symmetry plays a role and the group of the wave vector is modified as described above.

We must lastly consider the symmetry of $\Delta\eta'_{i,i}(\mathbf{r})$. The effective potential of the Wannier-like equation depends on $\Delta\eta$ and $\nabla(\Delta\eta)$, both of which are as symmetric as $\Delta\eta$

under rotary reflections. As a result, the point-group symmetry of $\Delta\eta'_{i,i}(\mathbf{r})$ is that of the defect perturbation $\Delta\eta(\mathbf{r})$. Labeling the point group symmetries of the defect perturbation as \mathcal{G}' , the symmetry of the Wannier-like equation for the envelope functions is then given by the point group generated by the symmetry elements of $\mathcal{G}' \cap \mathcal{G}'_{\mathbf{k}_i}$. Note that the point group \mathcal{G}' is independent of the photonic crystal lattice; the full point-group symmetry of the perturbed crystal (\mathcal{G}'') under which the localized states are classified is limited by the point group of the crystal (\mathcal{G}) and the position of the defect perturbation within the lattice.

The transformation properties of the *total* envelope, $\Gamma_{i,0}(\mathbf{r})e^{i\mathbf{k}_i \cdot \mathbf{r}}$, under the point-group symmetry operations of the localized defect in the lattice (\mathcal{G}''), are therefore identical to those of \mathbf{k}_i modulo a reciprocal-lattice vector. Point symmetries of the perturbed crystal which are in the group of the wave vector transform $\Gamma_{i,0}$ into itself, while all other point symmetries simply rotary reflect $\Gamma_{i,0}$ into $\Gamma_{j,0}$. In the context of a symmetry analysis of the mixing of states from different satellite points of the $^*\mathbf{k}$ then, one can neglect the transformation properties of the localized ground-state envelope functions since they transform effectively as the identity.

- *Electronic address: opainter@its.caltech.edu; <http://www.cco.caltech.edu/~aphome/painter.html>
- ¹D. M. Atkin, P. S. J. Russell, T. A. Birks, and P. J. Roberts, *J. Mod. Opt.* **43**, 1035 (1996).
 - ²P. S. J. Russell, D. M. Atkin, and T. A. Birks, *Bound Modes Of Two-Dimensional Photonic Crystal Waveguides* (Kluwer Academic, The Netherlands, 1996), pp. 203–218.
 - ³S. G. Johnson, S. Fan, P. R. Villeneuve, J. D. Joannopoulos, and L. A. Kolodziejaki, *Phys. Rev. B* **60**, 5751 (1999).
 - ⁴A. Mekis, J. C. Chen, I. Kurland, S. Fan, P. R. Villeneuve, and J. D. Joannopoulos, *Phys. Rev. Lett.* **77**, 3787 (1996).
 - ⁵E. Chow, S. Y. Lin, J. R. Wendt, S. G. Johnson, and J. D. Joannopoulos, *Opt. Lett.* **26**, 286 (2001).
 - ⁶T. Baba, N. Fukaya, and J. Yonekura, *IEE Electron Lett.* **35**, 654 (1999).
 - ⁷M. Lončar, T. Doll, J. Vučković, and A. Scherer, *J. Lightwave Technol.* **18**, 1402 (2000).
 - ⁸A. Yariv, Y. Xu, R. K. Lee, and A. Scherer, *Opt. Lett.* **24**, 711 (1999).
 - ⁹S. Olivier, C. Smith, M. Rattier, H. Benisty, C. Weisbuch, T. Krauss, R. Houdré, and U. Oesterlé, *Opt. Lett.* **26**, 1019 (2001).
 - ¹⁰C. Smith, R. De la Rue, M. Rattier, S. Olivier, H. Benisty, C. Weisbuch, T. Krauss, U. Oesterlé, and R. Houdré, *Appl. Phys. Lett.* **78**, 1487 (2001).
 - ¹¹S. Fan, P. R. Villeneuve, and J. D. Joannopoulos, *Opt. Express* **3**, 4 (1998); <http://www.opticsexpress.org/abstract.cfm> URI = OPEX-3-1-4.
 - ¹²S. Noda, A. Chutinan, and M. Imada, *Nature (London)* **407**, 608 (2000).
 - ¹³J. S. Foresi, P. R. Villeneuve, J. Ferrera, E. R. Thoen, G. Steinmeyer, S. Fan, J. D. Joannopoulos, L. C. Kimerling, H. I. Smith, and E. P. Ippen, *Nature (London)* **390**, 143 (1997).
 - ¹⁴O. Painter, J. Vučković, and A. Scherer, *J. Opt. Soc. Am. B* **16**, 275 (1999).

- ¹⁵R. Coccioli, M. Boroditsky, K. M. Kim, Y. Rahmat-Samii, and E. Yablonovitch, *IEE Proc.: Optoelectron.* **145**, 391 (1998).
- ¹⁶O. Painter, R. K. Lee, A. Yariv, A. Scherer, J. D. O'Brien, P. D. Dapkus, and I. Kim, *Science* **284**, 1819 (1999).
- ¹⁷O. Painter, A. Husain, A. Scherer, P. T. Lee, I. Kim, J. D. O'Brien, and P. D. Dapkus, *IEEE Photonics Technol. Lett.* **12**, 1126 (2000).
- ¹⁸O. Painter, K. Srinivasan, J. D. O'Brien, A. Scherer, and P. D. Dapkus, *J. Opt. A, Pure Appl. Opt.* **3**, S161 (2001).
- ¹⁹K. Srinivasan and O. Painter, *Opt. Express* **10**, 670 (2002).
- ²⁰P. Barclay, K. Srinivasan, M. Borselli, and O. Painter, *IEEE-Electron. Lett.* **39**(11), May 29 (2003).
- ²¹O. J. Painter, Ph.D. thesis, California Institute of Technology, 2001.
- ²²K. Sakoda, *Phys. Rev. B* **52**, 7982 (1995).
- ²³W. Ludwig and C. Falter, *Symmetries in Physics: Group Theory Applied to Physical Problems*, 2nd ed., Springer Series in Solid-State Sciences, Vol. 64 (Springer-Verlag, New York, 1996).
- ²⁴G. H. Wannier, *Rev. Mod. Phys.* **34**, 645 (1962).
- ²⁵J. D. Joannopoulos, R. D. Meade, and J. N. Winn, *Photonic Crystals* (Princeton University, Princeton, NJ, 1995).
- ²⁶O. J. Painter, A. Husain, A. Scherer, J. D. O'Brien, I. Kim, and P. D. Dapkus, *J. Lightwave Technol.* **17**, 2082 (1999).
- ²⁷In this calculation a 2D hexagonal PC with a host dielectric constant given by the effective index of the fundamental TE mode of the half-wavelength thick slab is analyzed (Ref. 14).
- ²⁸M. Tinkham, *Group Theory and Quantum Mechanics*, International Series in Pure and Applied Physics (McGraw-Hill, New York, 1964).
- ²⁹For the highly localized defect cavities studied here the energy associated with the curvature of a higher-order envelope function within the defect region is on the order of the energy associated with the Bloch part of the field.

- ³⁰As a result of nonidealities in the fabrication process (Ref. 26), the air holes near the center of the cavity are larger than those at the perimeter in the fabricated devices. A linear grading of the hole radius of 10% is quite common.
- ³¹Careful inspection of the FDTD generated magnetic-field plot for these two modes shows that the mode patterns appear to have lower symmetry than that quoted in the text. This is a consequence of the way in which the modes were simulated, using vertical mirror planes to reduce the computation domain by a factor of 4. Due to discretization of the computation grid, the mirror symmetry distorts the structure ever so slightly, resulting in a distortion of the field pattern. Simulations of the full structure do not show such distortions in the field patterns which have the full symmetry afforded by the C_{6v} point group.
- ³²O. Painter and K. Srinivasan, *Opt. Lett.* **27**, 339 (2002).
- ³³P. R. Villeneuve, S. Fan, S. G. Johnson, and J. D. Joannopoulos, *IEE Proc.: Optoelectron.* **145**, 384 (1998).
- ³⁴J. M. Luttinger and W. Kohn, *Phys. Rev.* **97**, 869 (1955).
- ³⁵C. Kittel and A. H. Mitchell, *Phys. Rev.* **96**, 1488 (1954).
- ³⁶O. Painter and K. Srinivasan (unpublished).
- ³⁷P. C. Sercel and K. J. Vahala, *Phys. Rev. B* **42**, 3690 (1990).
- ³⁸W. Kohn and J. M. Luttinger, *Phys. Rev.* **98**, 915 (1955).
- ³⁹A. Baldereschi, *Phys. Rev. B* **1**, 4673 (1970).
- ⁴⁰This can be checked for the representation of the l th band using the Herring criteria (Ref. 23).